Impact of different sources of precursors on a high-ozone event over Europe analysed with IASI+GOME2 multispectral satellite observations and model simulations

Sachiko Okamoto[1], Juan Cuesta[1], Matthias Beekmann[2], Gaëlle Dufour[2], Maxim Eremenko[1], Kazuyuki Miyazaki[3], Cathy Bonne[4], Hiroshi Tanimoto[5], Hajime Akimoto[5]

[1] Univ Paris Est Creteil and Université de Paris Cité, CNRS, LISA, F-94010 Créteil, France
[2] Université de Paris Cité and Univ Paris Est Creteil, CNRS, LISA, F-75013 Paris, France
[3] Jet Propulsion Laboratory (JPL), California Institute of Technology, Pasadena, 91109, CA, USA
[4] Institut Pierre Simon Laplace (IPSL), AERIS data centre, Paris, 75252, France
[5] National Institute for Environmental Studies, Tsukuba, 350-8506, Japan

Correspondence to: Sachiko Okamoto (sachiko.okamoto@lisa.ipsl.fr) and Juan Cuesta (cuesta@lisa.ipsl.fr)

Abstract. We examine the impact of different sources of ozone precursors on the daily evolution of successive major ozone pollution outbreaks across Europe in July 2017 by using a multispectral satellite approach called IASI+GOME2, and a tropospheric chemistry reanalysis called TCR-2. IASI+GOME2, combining IASI and GOME-2 measurements respectively in the infrared and the ultraviolet, allows the observation of the daily horizontal distribution of ozone in the lowermost troposphere (defined here as the atmospheric layer between the surface and 3 km above sea level). IASI+GOME2 observations show a fair capacity to depict near-surface ozone evolution as compared to surface measurements from 188 European stations for the period 15–27 July 2017.

At the beginning of this event (on 16 July), a major ozone outbreak is initially formed over the Iberian Peninsula likely linked with high temperature-induced enhancements of biogenic volatile organic compounds concentrations and collocated anthropogenic emissions. In the following days, the ozone plume splits into two branches, one being transported eastward across the Western Mediterranean and Italy, and the other one over Western and Central Europe. The southern branch encounters ozone precursors emitted over the Balkan Peninsula by wildfires along the coast of the Adriatic Sea and biogenic sources in the inland region of the Peninsula. Ozone concentrations of the northern plume enhance by photochemical production associated with anthropogenic sources of ozone precursors over Central Europe and by mixing with an ozone plume arriving from the North Sea that was originally produced over North America. Finally, both ozone branches are transported eastwards and mix gradually, as they reach the northern coast of the Black Sea. There, emissions from agricultural fires after harvesting clearly favor photochemical production of ozone within the pollution plume, which is advected eastwards in the following days. Based on satellite analysis, this paper shows the interplay of various ozone precursor sources to sustain a two-week long ozone pollution event over different parts of Europe.

1 Introduction

Tropospheric ozone is one of the key gases in the Earth's atmosphere because it plays a significant role in global warming (Szopa et al., 2021) and in determining the oxidizing capacity of the troposphere (Monks et al., 2015). Tropospheric ozone is also recognized as the gaseous air pollutant that causes the greatest threat to human and ecosystem health (Monks et al., 2015). The lifetime of ozone in the troposphere ranges from a few hours in polluted urban regions to up to few months in the upper troposphere, but it is in average relatively long (~22 days; Young et al., 2013). This allows tropospheric ozone transport over distances of intercontinental and hemispheric scales. The main sources of tropospheric ozone are in situ photochemical production through oxidation of non-methane volatile organic compounds (NMVOCs), carbon monoxide (CO) and methane (CH_4), in the presence of nitrogen oxides (NO_X) (e.g., Atkinson, 2000) and stratosphere-to-troposphere transport (e.g., Stohl et al., 2003). Photochemical formation of ozone occurs through a series of complex, nonlinear reactions involving sunlight, NO_X, volatile organic compounds (VOCs), and oxidation of free radical species (Chameides and Walker, 1973). Generally, local concentrations of either radicals or NO_X are sufficiently high so that the other species are chemically limiting the formation of ozone. These two photochemical regimes are commonly referred to NO_X-limited and VOC-limited (NO_X-saturated or radical-limited) (Sillman et al., 1990; Kleiman, 1994). At regional and global scales, ozone production is largely NO_X-limited, although urban areas with high NO_X emissions are frequently VOC-limited. However, the sensitivity of local ozone production for individual locations and events is often uncertain. Understanding the complex spatial and temporal evolution of photochemical regimes at local scales is still an important issue.

The magnitude of local air pollution is strongly driven by local and regional emissions of air pollutants and their precursors. The precursors of ozone are emitted from multiple sources associated with anthropogenic activities, biogenic origin and biomass fires. In Europe, regional anthropogenic emissions have been controlled by governmental regulations and dropped considerably between 1990 and 2018 (EEA, 2020). NO_X emissions decreased (–60 %) in the electricity/energy generation sectors because of certain technical measures such as the introduction of combustion modification technology, the implementation of fuel gas abatement techniques, and fuel switching from coal to gas. NMVOCs emissions also decreased (–62 %) in the road transport sector. As a result of these reductions, the percentage of European Union (EU) urban population potentially exposed to high ozone concentrations (above the EU target value for protecting human health) have declined from 2002 to 2011 (Guerreiro et al., 2014). Additionally, summer peaks of ozone concentrations have also reduced over rural areas of Europe (~0.46 ppb yr^{-1} from 1995 to 2014; Yan et al., 2018). However, background ozone concentrations (5th percentile) have increased continually over Europe during the last years (~0.15 ppb yr^{-1}; Yan et al., 2018; 2019). This may be partly linked with enhancements of ozone levels in urban areas owing to a reduction of the urban ozone sink by titration, which is associated with the reduction of NO_X (Sicard et al., 2013; Yan et al., 2018; 2019). Moreover, the amount of ozone production not only responds nonlinearly to changes in precursor emissions but also it is sensitive to variations in air temperature, radiation, and other climate factors (e.g., Jacob and Winner, 2009). Especially, the impacts of temperature on ozone occur both directly and indirectly. The relationship between ozone and the precursors is driven by several well-known temperature-dependent

65 mechanisms: the thermal decomposition of the NO_X reservoir species peroxyacetyl nitrate (PAN, $CH_3COO_2NO_2$) (Orlando et al., 1992), the temperature-dependent emissions of both VOCs from vegetation and NO_X from soil (Vautard et al., 2005), the extra evaporation of anthropogenic VOCs at high temperature (Fehsenfeld et al., 1992; Simpson, 1995), or the high stomatal resistance in warm conditions, which limits the dry deposition of ozone on vegetation (Solberg et al., 2008).

Satellite observations offer a great potential for overcoming the limited spatial coverage of ground-based measurements and
70 filling the observational gap of air pollution. Nevertheless, measuring ozone pollution from space has been a challenge because standard single-band ozone retrievals cannot provide quantitative information of the ozone concentrations within the planetary boundary layer (PBL). Spaceborne spectrometers operating in the ultraviolet (UV), like GOME-2 (Global Ozone Monitoring Experiment-2), have been used to derive observations of tropospheric ozone with maximum sensitivity around 5–6 km altitude (e.g., Liu et al., 2010; Cai et al., 2012). Thermal infrared (TIR) spaceborne instruments, like IASI (Infrared Atmospheric
75 Sounding Interferometer) onboard the MetOp satellites, have shown good performance for observing ozone in the lower troposphere, but with sensitivity peaking at 3 km altitude at the lowest (e.g., Eremenko et al., 2008; Dufour et al., 2012). Recently, synergetic approaches simultaneously using UV and TIR radiances has been developed for enhancing the sensitivity to lower tropospheric ozone (e.g., Cuesta et al., 2013; Fu et al., 2013; 2018; Colombi et al., 2021). A multispectral approach called IASI+GOME2, combining IASI observations in the TIR and GOME-2 measurements in the UV, showed remarkable
80 skills for observing the horizontal distribution of ozone concentrations in the lowermost troposphere (LMT), hereafter defined as the atmospheric layer between the surface and 3 km above sea level (a.s.l.) (Cuesta et al., 2013; 2018). Cuesta et al. (2018) showed that IASI+GOME2 has air-quality-relevant skills to quantitatively describe the transport pathways, the daily evolution and photochemical production of lowermost tropospheric ozone during a major outbreak across East Asia.

In the present paper, we characterize a major ozone outbreak across Europe in July 2017 by using the multispectral satellite
85 approach IASI+GOME2, tropospheric chemistry reanalyses and other observations. We analyse the sources that have most probably contributed to ozone photochemical production along transport of major ozone plumes travelling from Southwest to Eastern Europe. To the authors' knowledge, such detailed identification of the sources of ozone precursors of a complex event over Europe has not yet been performed using satellite observations. Section 2 describes the observational and modelling data used for the analysis. Results and discussions on the evolution of the European ozone outbreak and the associated precursor
90 sources are presented in section 3. A summary and conclusions are given in the last section.

2 Data and methods

2.1 Satellite observations of lowermost tropospheric ozone from IASI+GOME2

The multispectral satellite approach IASI+GOME2 was designed for observing lowermost tropospheric ozone by synergism of TIR atmospheric radiances observed by IASI and UV earth reflectances measured by GOME-2 (Cuesta et al., 2013; 2018).
95 Both instruments are onboard the MetOp satellite series, and they both offer global coverage every day (for MetOp-A around

09:30 local time and for MetOp-B around 09:00 local time) with a relatively fine ground resolution (12 km diameter pixels spaced by 25 km for IASI at nadir and ground pixels of 80 km × 40 km for GOME-2). The IASI+GOME2/MetOp-B product including vertical profiles of ozone is publicly available on the French data centre AERIS (https://iasi.aeris-data.fr, last access: 7 November 2022). We use an updated version of the IASI+GOME2 product, merging the IASI+GOME2/MetOp-A and
100 IASI+GOME2/MetOp-B products for improving the spatial coverage. For reducing random errors, the dataset is averaged in a regular horizontal grid of 1° × 1°. Ozone concentrations from the surface to 3 km of altitude (a.s.l.) are provided as volume mixing ratio in ppb (parts per billion), calculated as the ratio of lowermost tropospheric partial columns (in molecules per square centimetre) of ozone and air. Hereinafter, this amount is designated as IASI+GOME2 LMT ozone concentration.

For assessing the contribution of IASI+GOME2 for capturing near surface ozone evolution, we compared IASI+GOME2 with
105 the surface observations of ozone in Europe. We consider hourly surface data from stations in rural areas, obtained from the Global Atmosphere Watch (GAW, http://ebas.nilu.no, last access: 28 January 2020), the European Monitoring and Evaluation Programme (EMEP, http://ebas.nilu.no, last access: 28 January 2020), and the European Air Quality e-Reporting (https://eea.europa.eu, last access: 27 January 2020). We identify rural stations based on the Tropospheric Ozone Assessment Report (TOAR) station category (Schultz et al., 2017). TOAR is a research community with an up-to-date scientific assessment
110 of tropospheric ozone's global distribution and trends from the surface to the tropopause initiated by the International Global Atmospheric Chemistry (IGAC). The TOAR station category characterizes stations as "urban", "rural, low elevation" (located below 1500 m a.s.l.), "rural, high elevation" (above 1500 m a.s.l.) and "unclassified" based on several high-resolution global gridded data products. Here we only use data from "rural, low elevation" and "rural, high elevation" stations. We consider afternoon averages (12:00–16:00 local time - LT) of these surface concentrations that are expected to be vertically mixed
115 within the mixing boundary layer. This is likely more comparable to IASI+GOME2 retrievals, that mainly measure ozone concentrations at the residual atmospheric boundary layer, than morning surface concentrations that have not been mixed within the whole boundary layer (Cuesta et al., 2022).

The comparison of IASI+GOME-2 data with respect to surface measurement is presented in Figure 1–2 and Table 1, for the period 15–27 July 2017 over Europe. We consider 188 stations (18 high elevation and 170 low elevation stations) in three
120 regions defined as shown in Fig. 1: Iberian Peninsula (39°–42°N, 0°–8°W), Southern and Central Europe (41°–48°N, 3°W–13°E), and Central and Eastern Europe (45°–50°N, 10°–25°E). Figure 1 shows the distribution of correlation coefficients for IASI+GOME2 with respect to in situ observations. Generally, the correlation coefficients are positive, with approximately 54% of the sites having statistically significant correlations (p < 0.05). Relatively higher correlation coefficients are found in the Western Mediterranean Basin, Central France, and Austria, whereas they are relatively lower over Western Iberian
125 Peninsula, North-western France and the Central Mediterranean Basin. Figure 2 shows the scatter plots for IASI+GOME2 with respect to in situ observations in three regions. All comparisons show significant correlations (p < 0.01). IASI+GOME2 over the Iberian Peninsula has a slight positive difference of 0.9 ppb. Over Southern and Central Europe and Central and Eastern Europe, the satellite retrievals are lower than in situ measurements by –4.7 ppb and –10.8 ppb, respectively. The root

mean squared (RMS) difference over the Iberian Peninsula is smaller than those in the other two regions. The values of
130 correlation coefficients around ~0.45 are not very high, but they may reflect differences in the spatio-temporal representativity
of surface in situ measurements and satellite data at daily scale and this particular event. Vertical gradients of ozone
concentrations near the surface may also be responsible of the apparent differences between satellite and surface data. Lower
ozone abundances retrieved by the satellite approach may be induced by high ozone concentrations near the surface, as
typically remarked during ozone outbreaks of anthropogenic origin. Previous comparisons of IASI+GOME2 data with surface
135 in situ measurements showed relatively larger values of correlation coefficients, being ~0.69 for a major ozone outbreak over
Eastern Asia (11 surface stations over Japan, Cuesta et al., 2018) and ~0.55 for differences of 15-day averages over Europe
(Cuesta et al., 2022). In this last case, ozone satellite retrievals over Europe are also lower than surface concentrations (by –
8.6 ppb over the whole continent).
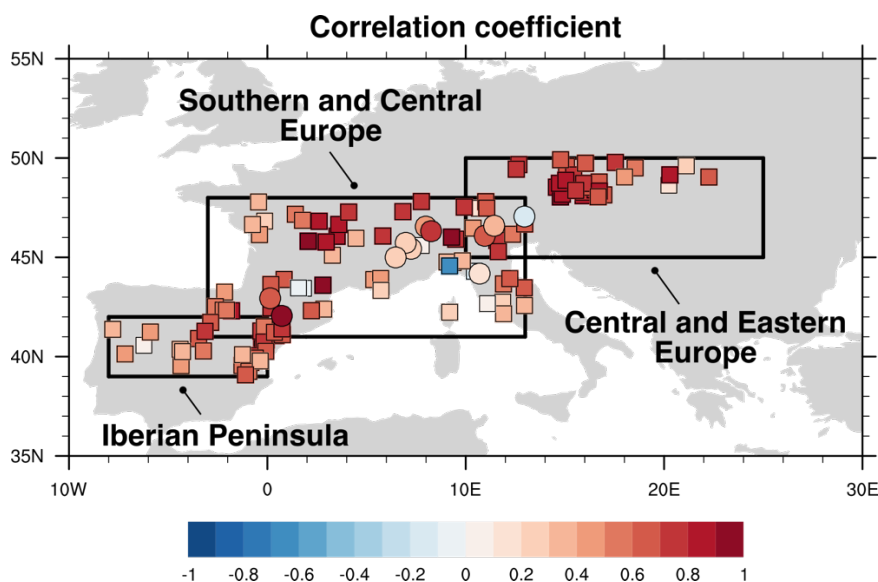
140

Figure 1: Distribution of correlation coefficients between IASI+GOME2 and observed surface ozone for the period 15–27 July 2017. Circles
and squares indicate high (above 1500 m a.s.l.) and low elevation stations based on the TOAR category, respectively. Black rectangles
indicate the subregions that were used for the comparisons of IASI+GOME2 and surface data (Fig. 2).
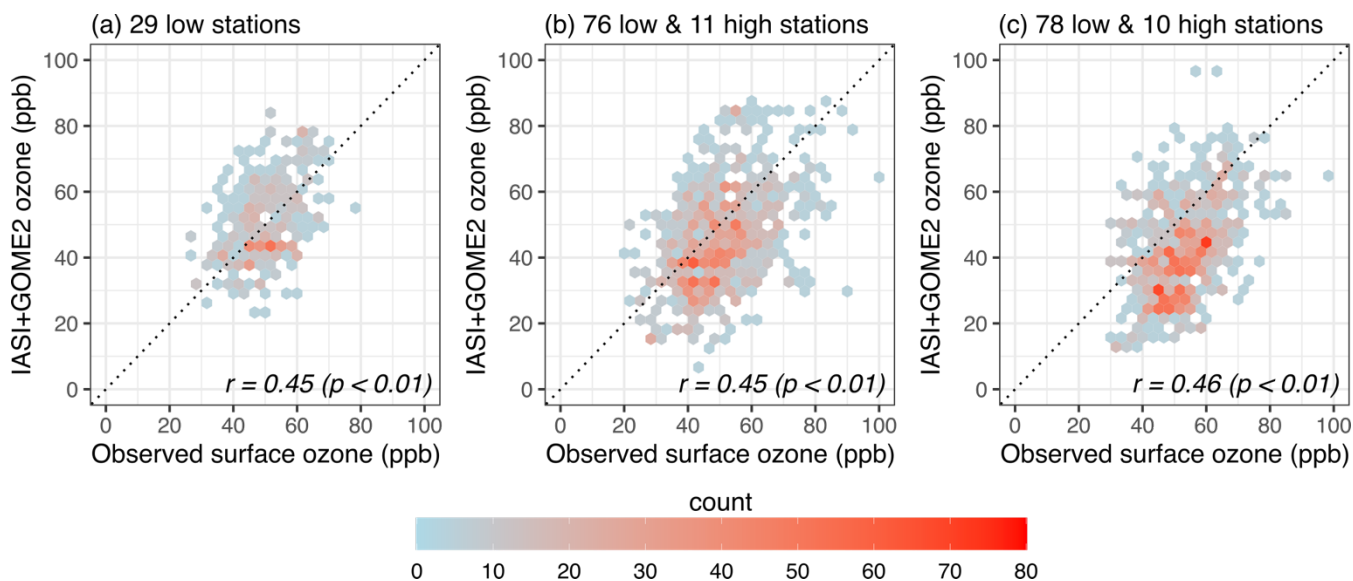
Figure 2: Comparison of IASI+GOME2 with surface observations of ozone for the period 15–27 July 2017. Scatter plots of IASI+GOME2 versus surface ozone in situ measurements over **(a)** the Iberian Peninsula, **(b)** Southern and Central Europe, and **(c)** Central and Eastern Europe.

Table 1: Statistics of comparison of in situ surface observations with respect to IASI+GOME2 ozone in three regions for the period 15–27 July 2017.

	Iberian Peninsula	Southern and Central Europe	Central and Eastern Europe
Mean difference (ppb)	0.9	–4.7	–10.8
RMS difference (ppb)	11.8	15.1	16.9
R	0.45 (p < 0.01)	0.45 (p < 0.01)	0.46 (p < 0.01)

2.2 Tropospheric Chemistry Reanalysis version 2 (TCR-2)

Chemical reanalyses provide comprehensive information on the evolution of atmospheric composition, offering the spatio-temporal full coverage of chemistry-transport models and enhanced precision by assimilation of various satellite observations. TCR-2 is a tropospheric chemical reanalysis based on an assimilation of multi-constituent observations from diverse satellite sensors (Miyazaki et al., 2020). TCR-2 data is publicly available for the period 2005–2019 (https://tes.jpl.nasa.gov/tes/chemical-reanalysis/). In the present study, we use 2-hourly TCR-2 reanalysis data (Miyazaki, personal communication, 2020) of ozone and two species representative of ozone precursors: nitrogen dioxide (NO_2) and

160 formaldehyde (HCHO) as proxy for NO_X and VOCs distributions, which provide supplemental information on the evolution and origin of anthropogenic air pollution.

TCR-2 uses MIROC-CHASER (Watanabe et al., 2011) as a base forecast model, which contains detailed photochemistry in the troposphere and stratosphere by simulating tracer transport, wet and dry depositions, and emissions. The model calculates the concentrations of 92 chemical species and 262 chemical reactions (58 photolytic, 183 kinetic, and 21 heterogeneous
165 reactions). Its tropospheric chemistry considers the fundamental chemical cycle of O_X-NO_X-HO_X-CH_4-CO along with oxidation of NMVOCs to properly represent ozone chemistry in the troposphere. TCR-2 has a T106 horizontal resolution (1.1° × 1.1°) with 32 vertical levels from the surface to 4.4 hPa. The simulated meteorological fields are nudged towards the 6-hourly ERA-Interim (Dee et al., 2011) to reproduce past meteorological fields. A priori emissions of NO_X, CO, and SO_2 are obtained from bottom-up emission inventories. Anthropogenic NO_X, CO and SO_2 emissions are obtained from the Hemispheric
170 Transport of Air Pollution (HTAP) v2 for 2010 (Janssens-Maenhout, et al., 2015). For biomass burning emissions, the monthly Global Fire Emissions Database (GFED) v4 (Randerson et al., 2018) are used. Emissions from soils are based on monthly mean Global Emissions Inventory Activity (GEIA) (Graedel et al., 1993). Data assimilation is based on an ensemble Kalman filter (EnKF) approach, the Local Ensemble Transform Kalman Filter (LETKF) (Hunt et al., 2007) for ozone (O_3), CO, NO_2, HNO_3 and SO_2. Tropospheric NO_2 column retrievals used for data assimilation are the QA4ECV version 1.1 level (L2) product
175 for the Ozone Monitoring Instrument (OMI) (Boersma et al., 2017a), GOME-2 (Boersma et al., 2017b), and the Scanning Imaging Absorption Spectrometer for Atmospheric Cartography (SCIAMACHY) (Boersma et al., 2017c). Ozone retrievals are taken from the version 6 level 2 nadir data obtained from the Tropospheric Emission Spectrometer (TES) (Bowman et al., 2006; Herman and Kulawik, 2020) and the version 4.2 for the Microwave Limb Sounder (MLS) for pressures of lower than 215 hPa (Livesey et al., 2011, 2020). Total column CO data are the version 7 L2 TIR/NIR product for the Measurements of
180 Pollution in the Troposphere (MOPITT) (Deeter et al., 2017). The performance of the chemical reanalysis products has been validated against various independent surface and aircraft measurements (Miyazaki et al., 2020). In this study, we use TCR-2 ozone at 850 hPa without smoothing by averaging kernel.

2.3 Other satellite observations and emission inventories

For analysing the origin and evolution of ozone plumes, CO retrievals from IASI/MetOp-B are used for identifying the location
185 of CO plumes. This total column CO product is publicly available at the French data centre AERIS (https://iasi.aeris-data.fr, last access: 7 November 2022). It is derived from IASI radiance using the FORLI algorithm (Fast Optimal Retrievals on Layer for IASI; Hurtmans et al., 2012), from the Université Libre de Bruxelles (ULB) and the Laboratoire Atmosphères, Milieux, Observations Spatiales (LATMOS). It is the same product used jointly with IASI+GOME2 data by Cuesta et al. (2018). For reducing random errors, the dataset was averaged in regular grid of 1° × 1° in the same way as IASI+GOME2. For consistency
190 with the other datasets, we derive CO mixing ratios assuming that all CO molecules within the column are located in the lowermost troposphere. Overestimations may occur for CO plumes extending above the LMT and because of the presence of

background CO in the free troposphere. This is not expected to impact our results, as these observations are mainly qualitatively used.

We analyse the sources of ozone precursors using anthropogenic and biogenic emissions from the Emissions of Atmospheric Compounds and Compilation of Ancillary Data (ECCAD, https://eccad.aeris-data.fr/, last access: 26 May 2021). Anthropogenic NO_X and NMVOCs emissions were obtained from CAMS Global anthropogenic emissions (CAMS-GLOB-ANT v4.2-S1.1; Granier et al., 2019). The emissions are based on the emissions provided by the Emissions Database for Global Atmospheric Research (EDGAR v4.3.2; Crippa et al., 2018) and the Community Emissions Data System (CEDS; Hoestly et al., 2018), and provided as monthly averages with a horizontal resolution of $0.1° \times 0.1°$. Soil NO emission was obtained from CAMS Global soil emissions provided as monthly averages with a horizontal resolution of $0.5° \times 0.5°$ (CAMS-GLOB-SOIL v2.3; Granier et al., 2019; Simpson and Darras, 2021). Soil NO_X is mainly emitted as NO. The Model of Emissions of Gases and Aerosols from Nature (MEGAN) is one of the most widely used biogenic emission model (Guenther et al., 2012). We obtained biogenic isoprene and monoterpenes emissions developed under the Monitoring Atmospheric Composition and Climate project (MACC), MEGAN-MACC Biogenic emission inventory (MACC-MEGAN, Sindelarova et al., 2014). The emissions are provided as monthly averages with a horizontal resolution of $0.5° \times 0.5°$.

The locations of fires are derived from the Terra and Aqua MODIS (Moderate Resolution Imaging Spectrometer) active fire products (MCD14ML Collection 6; Giglio et al., 2016) distributed by the Fire Information for Resources Management System (FIRMS, https://earthdata.nasa.gov/firms, last access: 13 March 2020). This dataset provides the values of Fire Radiative Power (FRP) and the inferred hot spot type: "presumed vegetation fire", "active volcano", "other static land source", and "offshore". We only used the FRP values of "presumed vegetation fire". In addition to the active fire product, we examine the type of fire with the Terra and Aqua combined MODIS Land Cover Climate Modeling Grid (CMG) (MCD12C1) Version 6 data product (Friedl and Sulla-Menashe, 2015). The global land cover is distributed by the Land Processes Distributed Active Archive Center (LP DAAC, https://lpdaac.usgs.gov/, last access: 25 May 2021) at yearly intervals with horizontal resolution of $0.05° \times 0.05°$. We adopt the International Geosphere-Biosphere Programme (IGBP) classification scheme.

2.4 Meteorological and trajectory analysis

Meteorological conditions leading to photochemical production of ozone and transport are described with ERA5 reanalysis (Hersbach et al., 2020) by the European Centre for Medium-Range Weather Forecast (ECMWF). These meteorological fields have global coverage, a horizontal resolution of $0.25° \times 0.25°$, 37 pressure levels and a time step of 1 hour (download from the Meso-centre IPSL through https://climserv.ipsl.polytechnique.fr, last access: 23 February 2021) and calculate several indices. Heatwaves are detected with a method adapted from Lavaysse et al. (2018), which is implemented in the Copernicus European Drought Observatory (EDO). This indicator is calculated from daily maximum 2 m temperature (T_{max}). The threshold values of T_{max} that characterize a heatwave are calculated from the observed T_{max} for the calendar day during the extended summer (April–October) for a 30-year baseline period (1981–2010). The daily threshold values for T_{max} are defined as the 90th

percentile of 330 respective temperature values in an 11-day window centred on that day, for all years in the baseline period.
225   A heatwave is detected when there are at least three consecutive days with T_{max} above its daily threshold value. When two
successive heatwaves are separated in time by one day, they are considered as a single event and merged.

A classification of air masses originated at low latitude subtropical desertic areas is performed according to a method proposed
by Sousa et al., (2019). The two following criteria identify the Saharan warm air intrusion: i) 1000–500 hPa layer geopotential
thickness larger than 5800 m, and ii) 925–700 hPa layer potential temperature (θ) greater than 40 °C. Grid points satisfying
230   both criteria correspond to low density, warm, stable, and very dry air masses, with the potential to be additionally warmed by
downward advection. For confirming the occurrence of Saharan air intrusions, we analyse measurements from the Aerosol
Robotic Network (AERONET) project, which is a ground-based aerosol remote sensing network (Holben et al., 1998). The
aerosol optical depth (AOD) level 2 data from the Version 3 product is publicly available (https://aeronet.gsfc.nasa.gov, last
access: 14 September 2020). The spectral variation of the AOD is expressed as the Angström exponent. This variable is known
235   as a qualitative indicator of aerosol particle size (Ångström, 1929); as small values (typically smaller than 0.5) indicate a
greater abundance of coarse aerosols, such as desert dust and sea salt, and larger values suggest the presence of fine aerosols,
typically from urban and biomass burning origins (e.g., Eck et al., 1999). This indicator is examined with measurements from
Madrid (40.452°N, 3.724°W) and Granada (37.164°N, 3.605°W).

Air stagnation is characterized by stable weather conditions and weak winds in the lower to mid-troposphere and absence of
240   precipitation. It is often defined by three meteorological variables: upper-air speed, near-surface wind speed and precipitation.
According to the previous method (Horton et al., 2012; Garrido-Perez et al., 2018, 2019), we considered a day and location as
stagnant when the three following criteria are fulfilled simultaneously: daily mean windspeeds lower than 3.2 and 13.0 m s⁻¹
respectively at i) 10 m and ii) 500 hPa, and iii) daily total precipitation less than 1.0 mm.

Pathways of polluted air masses transported across Europe are estimated by the National Oceanic and Atmospheric
245   Administration (NOAA) Hybrid Single Particle Lagrangian Integrated Trajectory (HYSPLIT) model (Draxler and Hess, 1997;
1998; Draxler, 1999; Stein et al., 2015), driven by Global Data Assimilation System (GDAS) meteorological simulations (1°
× 1° grid, from http://ready.arl.noaa.gov/archives.php, last access: 28 September 2020). We set the start height of calculation
to 3000 m a.s.l. (which is the top of the LMT).

3 Results and discussion

250   The major ozone outbreak travelling across Europe is formed by three ozone plumes originating from the Iberian Peninsula,
Western Europe and North America. Three-day forward trajectories from HYSPLIT depict the pathway of these ozone plumes
(Fig. 3). Figure 4 shows a quantitative analysis of the Lagrangian evolution of three ozone plumes which can be clearly
observed in IASI+GOME2 LMT ozone distributions for the period from 16 to 26 July 2017. These timeseries show the daily
evolution of a given variable averaged at the location of highlighted major ozone plumes (discussed in section 3.1 to 3.4 and

255   shown by red, blue, and black rectangles in Figs. 7, 9–11). These areas are defined according to the horizontal distributions of high concentrations of ozone depicted by IASI+GOME2 and forward trajectories. The ozone concentrations in the plumes are often near 90 ppb, corresponding to the ozone information threshold (whereby a 1-hour average concentration of 180 µg m^{-3} triggers an obligation to inform the population on possible risk; EC, 2008). The ozone concentrations of these plumes are clearly enhanced by four dominant sources of ozone precursors, identified in this study. A first ozone plume is formed on 16

260   July and lasts until the end of the events on 26 July (Fig. 3e–g and red lines in Fig. 4). The initial formation of this moderately dense ozone plume is likely associated with enhanced biogenic emissions during the first two days, as depicted by high concentrations of HCHO (red line in Fig. 4d). During this period, the ozone plume is co-located with low concentrations of CO, suggesting a limited influence of air pollutants emitted by combustion. Section 3.1 shows that this occurs over the Iberian Peninsula, where high surface temperature conditions prevail. In the following days, the ozone plume splits into two branches,

265   one being transported eastward across the Western Mediterranean and Italy, and the other one over Western and Central Europe (Fig. 3e). In addition to the plume formed over the Iberian Peninsula, two supplementary ozone plumes are formed on 17–18 July (Fig. 3a–d and black and blue lines in Fig. 4). Their increasing ozone concentrations are co-located with those of high CO content which clearly indicate a combustion-related origin of ozone precursors. As shown in section 3.2, the sources of these precursors are related to local anthropogenic activities in Southern and Central Europe (black lines in Fig. 4; subsection 3.2.1)

270   and transport of aged air masses from North America (blue lines in Fig. 4; subsection 3.2.2). On 21–22 July, the southern branch of the plume from the Iberian Peninsula is transported eastward across the North-western Mediterranean (Fig. 3f–g), exhibiting low concentrations of CO, NO$_2$ and HCHO (red line in Fig. 4c–e). The concentrations of these precursors increase as the plume approaches Italy and remain high while reaching the Balkan Peninsula. As shown in section 3.3, these last ones originate from wildfire emissions along the coast of the Adriatic Sea and biogenic emissions in the inland region of the Balkan

275   Peninsula. On 23 July, all ozone plumes mix into a single large plume, while they encounter very high CO concentrations (Fig. 3b, d and g). These CO emissions are associated with active agricultural burning over the north coast of the Black Sea, as described in section 3.4.
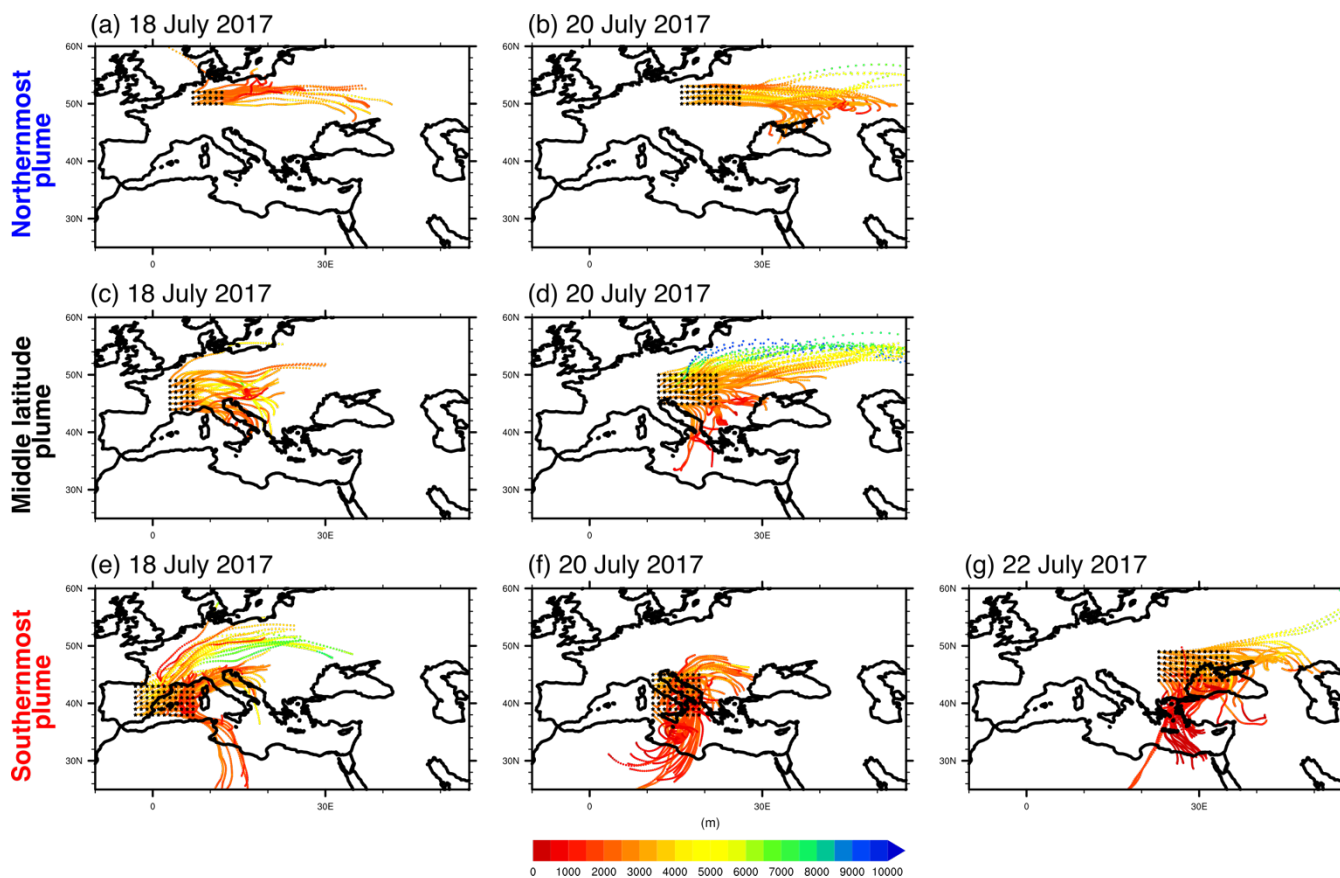
Figure 3: Three-day HYSPLIT forward trajectories depicting the pathways of the ozone plumes during the major ozone outbreak in July 2017 over Europe. The tracks followed by the northernmost, middle latitude, and southernmost ozone plumes are shown in the **(a and b)** upper, **(c and d)** middle and **(e, f and g)** lower panels. The trajectories start at 09:00 GMT on **(a, c and e)** 18, **(b, d and f)** 20 and **(g)** 22 July 2017, initiated at 3000 m (a.s.l.). Black points indicate the starting locations corresponding the locations of ozone plumes.
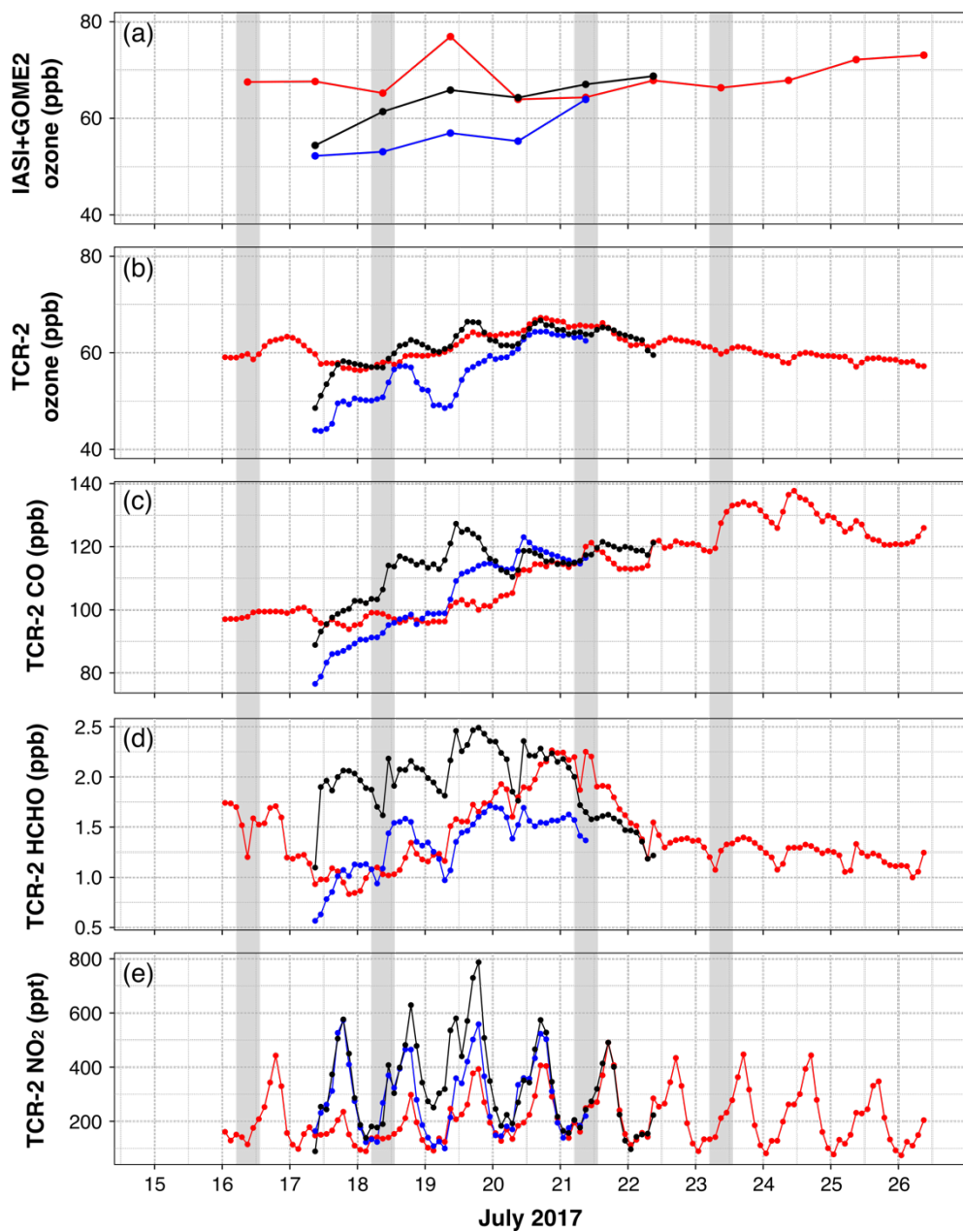
Figure 4: Lagrangian evolution of three air pollution plumes across Europe (rectangles in Figs. 7, 9–11) for the period from 16 to 26 July 2017 for the following variables:**(a)** lowermost tropospheric ozone from IASI+GOME2 and **(b)** ozone, **(c)** CO, **(d)** HCHO, and **(e)** NO_2 at 850 hPa from TCR-2. Red, blue, and black lines indicate the air pollution plumes from respectively the Iberian Peninsula, North America and western Europe, whose locations are depicted from the horizontal distribution of LMT ozone derived from IASI+GOME2. Gray shades indicate the date shown in Fig. 7, 9–11.

3.1 Ozone outbreak over the Iberian Peninsula

3.1.1 Meteorological conditions

As typically during summer, an elevated layer of warm, dry and dusty air called Saharan air layer (SAL) is transported over
295 the tropical Atlantic during the month of July 2017 (shown in Fig. S1 for 10 July 2017). The SAL is formed as warm and dry
Saharan air moves westwards off the African coast, which is undercut by oceanic cooler and moister air of the marine boundary
layer (see Fig. 5a–c, in similar conditions as described by e.g., Karyampudi and Carlson, 1988). While desertic air masses
typically remain over the Sahara and the Atlantic, distant from Europe, an anticyclone occurring in mid-July 2017 favours the
northward advection of these warm air masses. On 12 July, the high-pressure system is observed in terms of positive
300 geopotential height anomalies at 500 hPa over the Iberian Peninsula, Northern Africa and North Atlantic (see isolines of
geopotential height in Fig. 5d). On 13 and 14 July, the Saharan air intrusion reaches the Iberian Peninsula, as north as 40°N.
The arrival of these desertic air masses is confirmed by sun photometer observations depicting large amounts of coarse
particles, likely Saharan desert dust, over Central and Southern Iberian Peninsula (respectively at Madrid and Granada, Fig.
6c). This is suggested by low values of Ångström exponents measured on 11–19 July.

305
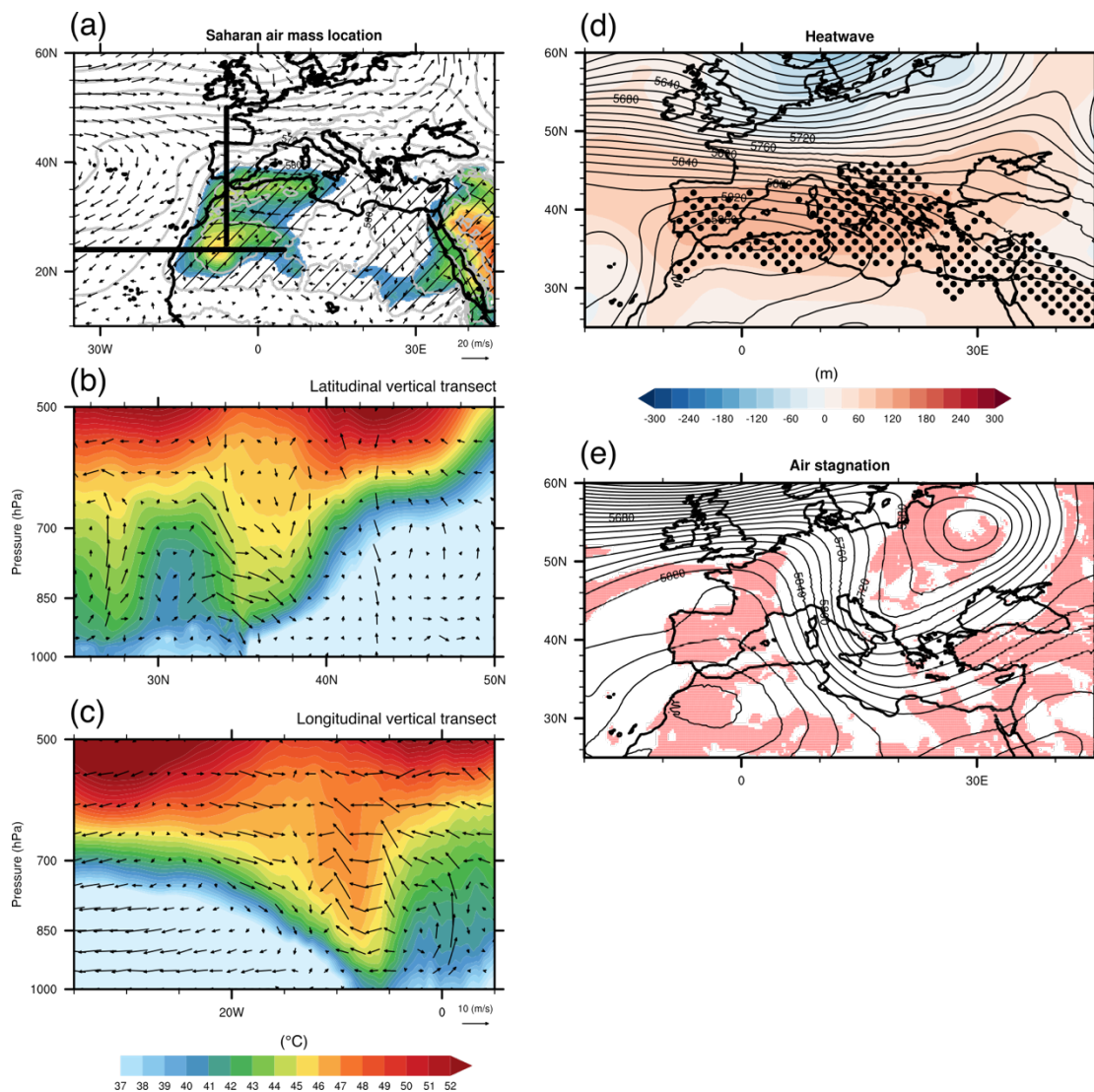
Figure 5: Meteorological conditions at the beginning of the ozone outbreak in July 2017. **(a)** Horizontal distribution of mean potential temperature from 925 hPa to 700 hPa and **(b–c)** transects of vertical profiles of potential temperature on 12 July 2017. Black bold straight lines and grey contours in panel (a) indicate the positions of respectively the transects of vertical profiles and daily mean geopotential height at 500 hPa. Black arrows in panels (b–c) indicate horizontal wind and vertical velocity. **(d)** Areas under heatwave conditions (black dot) on 12 July 2017, with black contour lines and colour shades indicating daily mean and daily anomaly of geopotential height at 500 hPa, respectively. **(e)** Regions under air stagnation conditions (light red shade) and daily mean geopotential height at 850 hPa (black contour lines) on 18 July 2017.

310
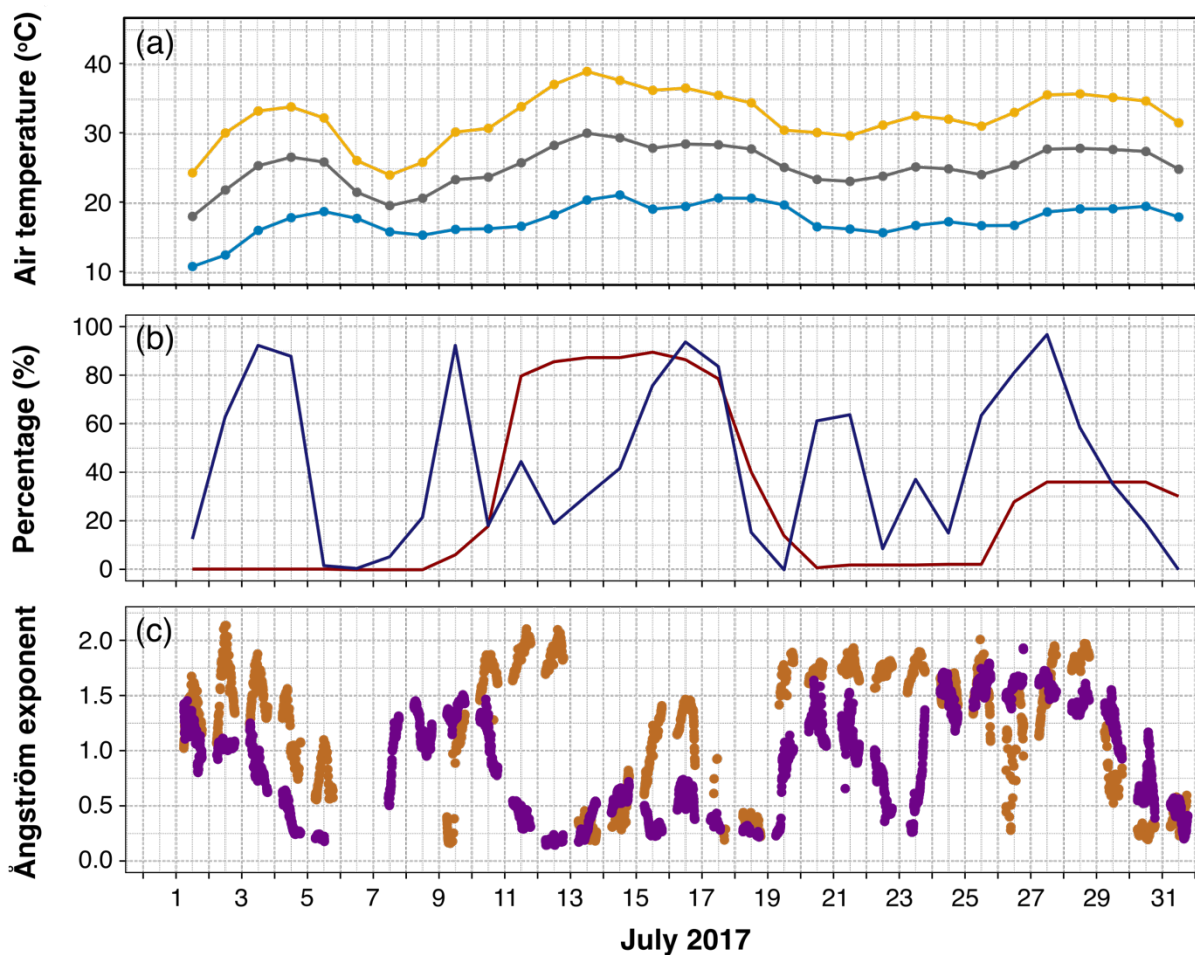
Figure 6: Meteorological conditions over the Central Iberian Peninsula (38–42°N, 2–7°W) in July 2017: **(a)** daily maximum (gold), mean (grey), minimum (blue) temperatures, **(b)** fractions of grid which satisfy the criteria for heatwave (dark red) and air stagnation (navy), and **(c)** Ångström exponents in Madrid (blown) and Granada (purple) (c).

The anticyclonic conditions and the arrival of Saharan air over the Iberian Peninsula induce heatwave conditions (see dots in Fig. 5d), that also reach the Eastern Mediterranean. Air temperatures over the Central Iberian Peninsula (38°–42°N, 2°–7°W, indicated in Fig. 4) start increasing in early July and reach a maximum on 13 July (see Fig. 6a). In Madrid, the surface air temperature reaches 40.6 °C on 13 July (Kew et al., 2019). The heatwave prevails over almost all the Central Iberian Peninsula from 11 to 18 July (see dark red line in Fig. 6b). This situation usually favours air subsidence, clear skies, and solar heating.

Typically, concomitant with anticyclonic conditions and heatwaves, air stagnation is an additional factor favoring the production and accumulation of air pollutants. This is also the case over the Iberian Peninsula on 15–17 July 2017 according to the air stagnation indicator shown in Fig. 6b. The anticyclone over Northern Africa likely plays a key role for air stagnation,

as it blocks the westerly flow, decreasing both near-surface and upper-air wind speed, and reducing precipitations. This situation continues until 18 July.

330 3.1.2 Photochemical production of ozone from biogenic emissions

These meteorological conditions remaining for over one week favour photochemical production of ozone and likely contributes to trigger the ozone outbreak over the Iberian Peninsula. On 16 July 2017, an enhancement of ozone concentration over the Iberian Peninsula is observed by IASI+GOME2 (red rectangle in Fig. 7a). The ozone plume is co-located with low CO concentrations for the period from 15 to 17 July (indicated in red line in Fig. 4 and Fig. 7a–c from TCR-2 reanalysis), indicating

335 minor influence of combustion-related emissions (typically from biomass burning and some anthropogenic activities). TCR-2 show an ozone plume over the Canary Islands on 12 July (not shown), which is transported along the edge of warm Saharan air, for arriving to Western Iberian Peninsula on 15–16 July (Fig. 7b). In addition, TCR-2 shows ozone plumes originating from North America that are transported across the North Atlantic for arriving to North-western Iberian Peninsula on 13–15 July (not shown). However, those ozone plumes transported to the Iberian Peninsula are only partially depicted by

340 IASI+GOME2 observations. These differences could be associated with misrepresentation of these ozone plumes in the simulations or lack of sensitivity (or spatial coverage) in the satellite data (particularly over the ocean). The 7-day back-trajectories confirm that the air masses come from the west over the North Atlantic and offshore transport from Western Africa in the middle troposphere (Fig. 7f). It suggests that the link between those ozone plumes and emissions in North America is unclear. Pay et al. (2019) showed that ground-level ozone concentrations over the Iberian Peninsula were strongly affected by

345 vertical mixing of ozone-rich layers during a high-ozone event in July 2012. The ozone concentration level over the Iberian Peninsula (over 70 ppb; Fig. 7a) is compatible with that in the middle troposphere (e.g., Petetin et al., 2016). Therefore, part of the ozone sources could be downward transport from the middle troposphere.
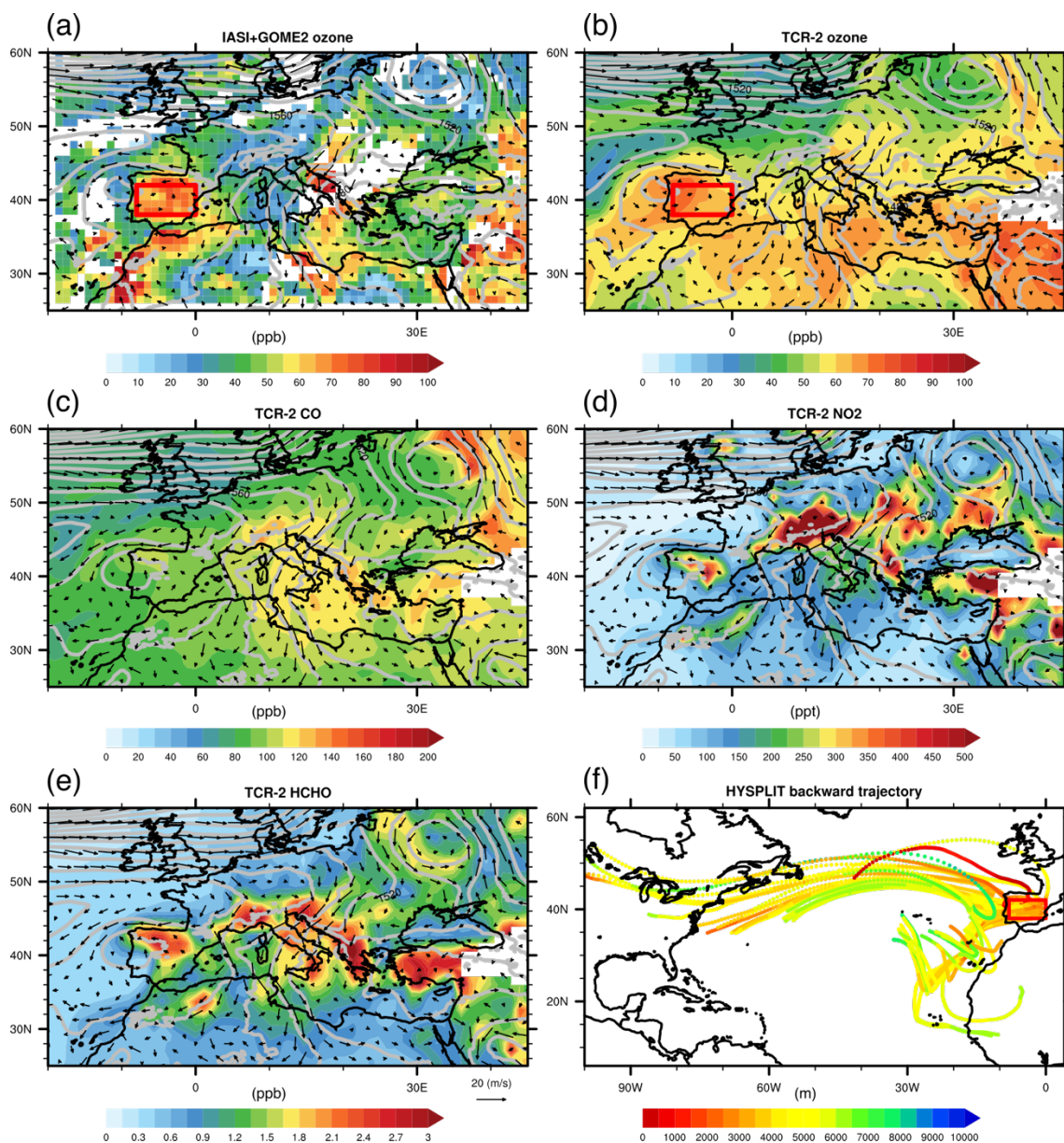
Figure 7: Distribution of gaseous pollutants and the meteorological conditions over Europe and the surrounding areas on 16 July 2017: **(a)** lowermost tropospheric ozone from IASI+GOME2 and **(b)** ozone, **(c)** CO, **(d)** NO₂, **(e)** HCHO from TCR-2 in the morning (at 09:00 GMT) at 850hPa, and **(f)** 7-day back trajectories arriving at 3000 m (a.s.l.) in the Iberian Peninsula. Winds and geopotential height at 850 hPa from ERA5 are indicated by black arrows and grey contour lines in panels (a–e). The red rectangles in (a–b) show the area for averaging concentrations of various air pollutants in Figure 2.

355

Meanwhile, enhanced concentrations of ozone precursors like NO₂ and HCHO are shown over Southern and Central Iberian Peninsula by the tropospheric reanalyses (Fig. 7d–e). These precursors are likely emitted locally, as their short lifetimes prevent the direct influence of long-range transport. The highest levels of NO₂ are seen over Madrid (the largest Spanish urban area)

and northwest from it (León and Palencia provinces), which is a region with significant mining and power generation industries
360 (Cuevas et al., 2014). The area with the highest levels of HCHO, which is the most important intermediate compounds in the
degradation of VOCs in the troposphere, extends over most of Spain (except for the south-eastern region). In addition, low
wind speed conditions may allow the accumulation of these ozone precursors.

Biogenic VOCs (BVOCs), dominated by isoprene and monoterpenes, are especially important for ozone production since they
are usually highly reactive. According to the MACC-MEGAN emission inventory in July 2017, biogenic emissions of isoprene
365 and monoterpenes are most abundant over the Mediterranean basin and moderate levels of monoterpenes over Central and
Eastern Europe (see Fig. 8c–d). This kind of biogenic emissions can significantly increase by high temperatures (Curci et al.,
2009), as those registered during the heatwave in July 2017. The impact of BVOCs on ozone production is likely important
over areas with major sources of NO_X, and thus low VOC-to-NO_X ratios, as over the Po Valley, North-eastern Spain and
Central Europe (Castell et al., 2008; Curci et al., 2009; Sartelet et al., 2012). Thus, we expect that the ozone plume over the
370 Iberian Peninsula is mainly associated with local biogenic emissions of VOCs collocated with large emissions of NO_X. Sources
of this last compound are probably soil related. According to CAMS-GLOB-ANT and CAMS-GLOB-SOIL emission
inventories (Fig. 8), the amounts of anthropogenic emissions of NO_X and soil emissions of NO are respectively 6.8 Gg and 5.8
Gg over Central Iberian Peninsula (38–42°N, 2–7°W) in July 2017. The relative contribution of soil NO emissions to the total
tropospheric NO_X budget would not be negligible, although a qualitative estimation would be difficult due to the large
375 uncertainties for their quantification (e.g., Hudman et al., 2012; Vinken et al., 2014). Relatively low CO abundances also
suggest that combustion emissions are not dominant.
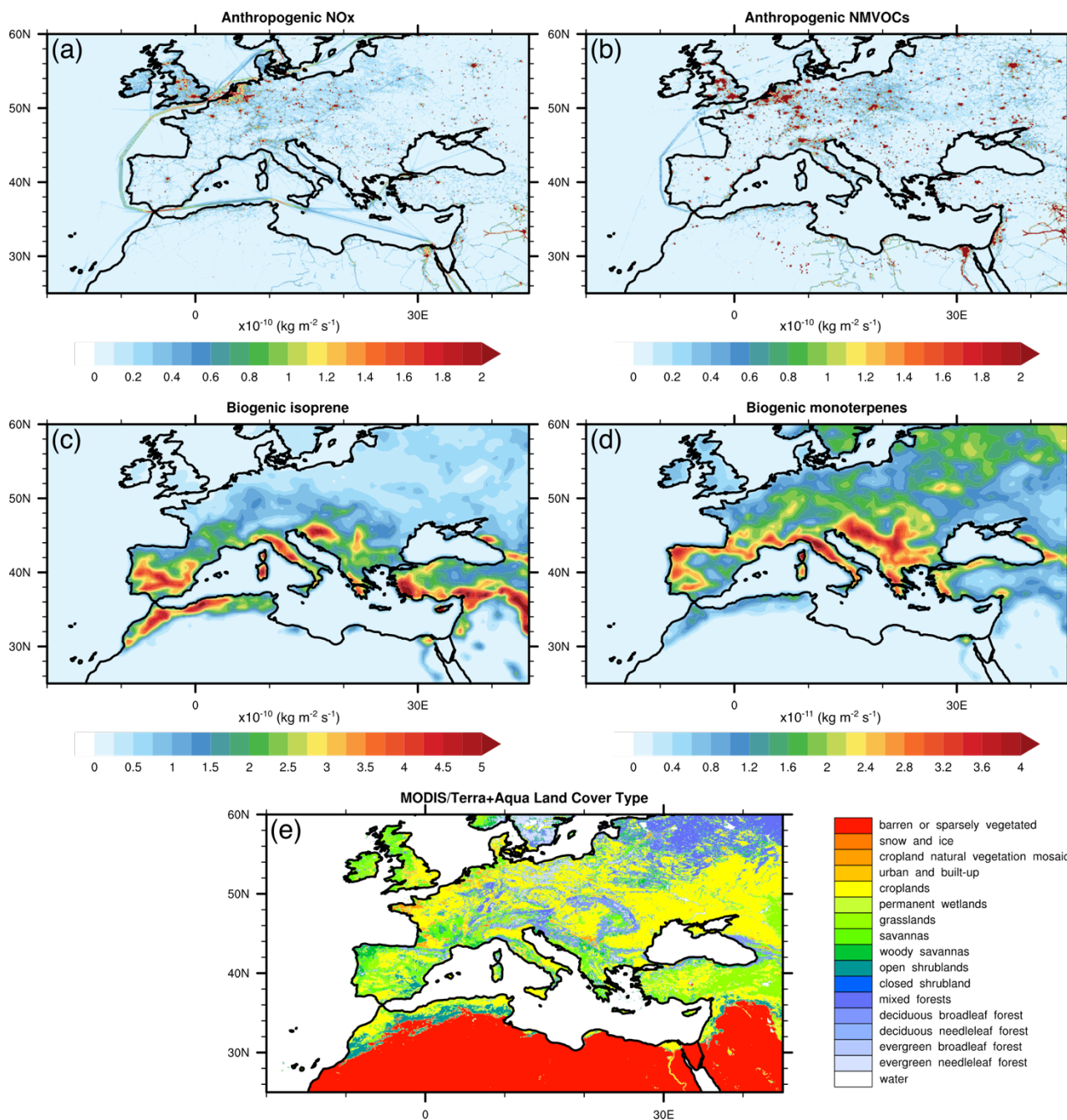
Figure 8: Horizontal distributions of anthropogenic and biogenic emissions, and land cover types over Europe and the surrounding regions. Monthly mean emissions of **(a)** anthropogenic NO$_X$ and **(b)** anthropogenic NMVOCs from CAMS-GLOB-ANT, and **(c)** biogenic isoprene and **(d)** biogenic monoterpenes from MEGAN-MACC in July 2017. **(e)** MODIS land cover types in 2017.

The current analysis suggests significant concomitant roles of the heatwave, air stagnation and high emissions of BVOCs contributing to the ozone outbreak over the Iberian Peninsula. In addition, this outbreak may also be affected by downward
385   transport from middle troposphere. However, it is difficult to quantitively evaluate the influence of each of them. Previous studies reported significant correlations between surface ozone abundance and the percentage of air stagnation in the Iberian Peninsula and other regions in Europe (Garrido-Perez et al., 2018, 2019), and in North America (e.g., Leibensperger et al., 2008). On the other hand, other studies over the United States suggest a minor role of high temperatures, since these conditions lasting several days do not result in a significant ozone increases in any region of this country (Sun et al., 2017).

390   **3.2 Impact of anthropogenic emissions in Western and Central Europe**

3.2.1 Local origin of an ozone plume in Western Europe

The ozone plume formed over the Iberian Peninsula splits into two branches. On 18 July, the northern branch of the plume is transported over Southern France (Fig. 3e and red rectangle in Fig. 9a). An additional dense ozone plume can also be identified over Eastern France by IASI+GOME2, in agreement with surface in situ measurements (black rectangle in Fig. 9a). In this
395   region, TCR-2 also simulates moderately high ozone concentrations at 850 hPa (black rectangle in Fig. 9b) and surface level (not shown). The tropospheric reanalysis also depicts a denser ozone plume over Northern Spain, Western France and the nearby Atlantic. This last one is not depicted by IASI+GOME2 at the LMT nor by in situ measurements at the surface. Ozone concentrations simulated at surface level (not shown) are rather moderate at this location, but higher over Eastern France, thus in better agreement with surface and satellite data. At the upper troposphere (between 6 and 12 km of altitude, not shown),
400   IASI+GOME2 does depict an ozone plume over Western France and located slightly north of the one simulated by TCR-2. This suggests uncertainties in the vertical and horizontal location of this lofted ozone plume in the model. It is worth noting that the satellite ozone observations assimilated in TCR-2 are derived from TES measurements with a coarse horizontal resolution (only nadir pointing) and most sensitivity to ozone at the Free troposphere at lowest.

405
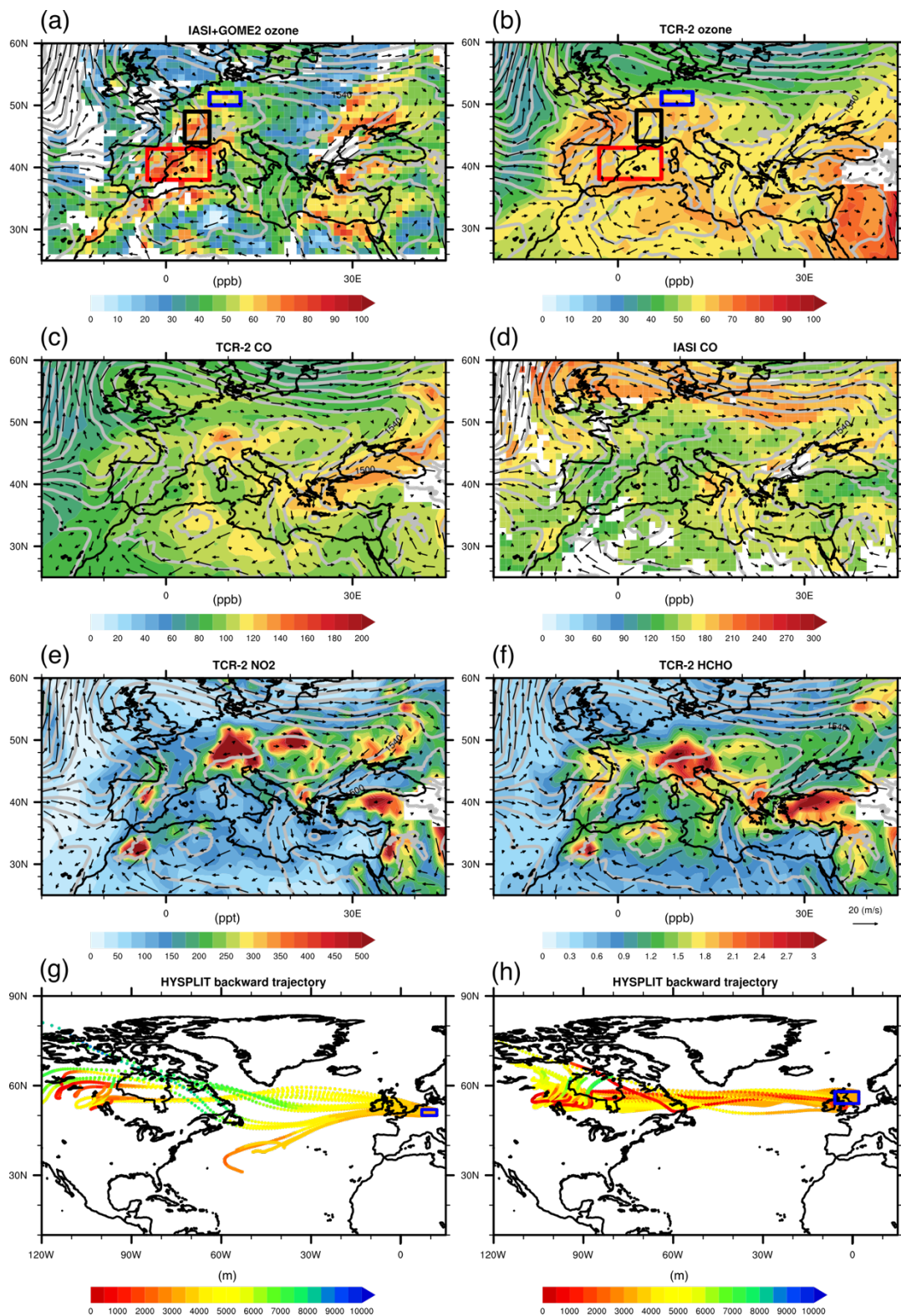
Figure 9: Distribution of gaseous pollutants and the meteorological situation over Europe and the surrounding areas on 18 July 2017: **(a)** lowermost tropospheric ozone from IASI+GOME2, **(b)** ozone, **(c)** CO, **(e)** NO$_2$, and **(f)** HCHO from TCR-2 at 850hPa and **(d)** CO from IASI in the morning (at 09:00 GMT). **(g–h)** Seven-day back trajectories arriving at 3000 m a.s.l. at the locations where ozone plumes are observed.

410

The ozone plume observed over Eastern France on 18 July (black rectangle in Fig. 9a) may partially originate from ozone and/or ozone precursors from the Iberian Peninsula, namely the northern branch of the ozone plume, according to forward trajectories from the previous day (not shown), which are similar to those on 18 July (Fig. 3e). However, this ozone-enriched air masses are co-located with clearly higher CO, NO$_2$ and HCHO concentrations (Figs. 9c–f) than those observed over the Iberian Peninsula the day before (and over Southern France on 18 July, red rectangle in Fig. 9a). These air pollutants are associated with a dense plume of CO, NO$_2$ and HCHO simulated by TCR-2 over Central Europe (including Eastern France). This suggests the influence of additional sources of these atmospheric constituents (whose evolution is shown by black lines in Fig. 4c–e). Anthropogenic emissions of NO$_X$ and particularly NMVOCs (Fig. 8a–b) clearly show hotspots over Central Europe (with populated urban areas and road transportation), according to the CAMS-GLOB-ANT inventory. Moderately high BVOC emissions (particularly monoterpenes, Fig. 8d) are also seen over Eastern France and larger ones over Southern France. These ozone precursors are transported westwards by easterly winds under anticyclonic conditions. We conclude that the ozone plume over Eastern France on 18 July is highly influenced by anthropogenic emissions from Central Europe, although not particularly from Eastern France itself (exhibiting lower anthropogenic emissions).

In the following days, the concentrations of ozone and its precursors within the plume in Central Europe gradually increase (black line in Fig. 4), while being transported eastwards (Fig. 3c–d). When the polluted plume passes over Northern Italy and Germany (not shown), it encounters large local anthropogenic emissions of precursors that probably mix within the plume. On 21 July, this pollution plume reaches Eastern Europe (extending from Hungary to Eastern Ukraine, see black rectangle in Fig. 10a).

430
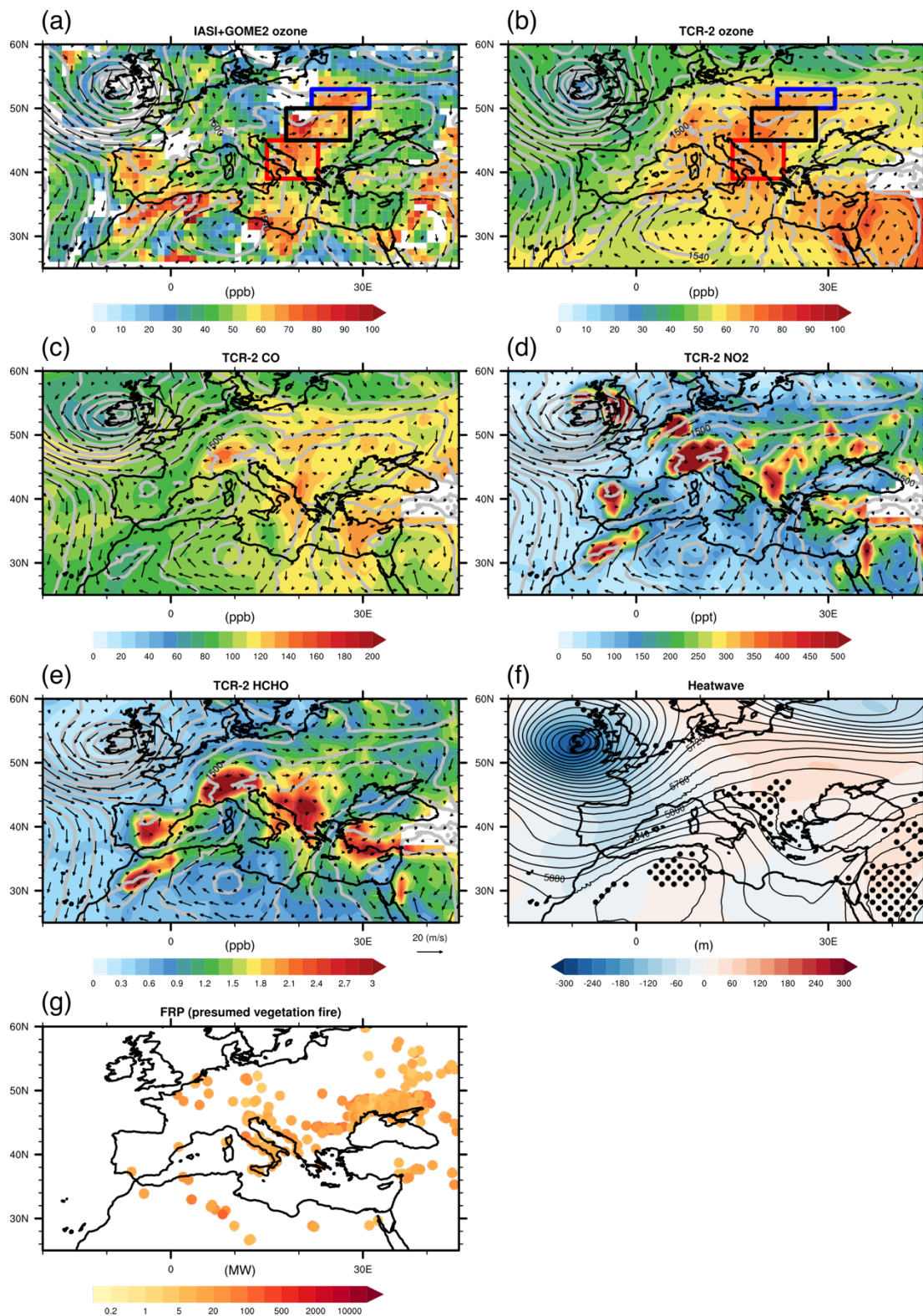
Figure 10: (a–e) Same as Fig. 7 but on 21 July 2017. **(f)** Heatwave indicators (black dots) and **(g)** fire radiative power (FRP) of presumed vegetation fire on 21 July 2017. Black contour lines and colour shades in (f) indicate daily mean and daily anomaly of geopotential height at 500 hPa, respectively.

435 3.2.2 Transatlantic transports from North America

Long-range transatlantic transport of air pollutants and their impact on air quality over Europe have been previously examined by using chemistry transport models, satellites, aircrafts and surface observations (e.g., Guerova et al., 2006; Li et al., 2002; Val Martin et al., 2006). Guerova et al. (2006) estimated that the contribution of ozone from North America to Europe ranged from 3–5 ppb in the planetary boundary layer and 10–13 ppb in the middle and upper troposphere in summer.

440 During the analysed period in July 2017, an ozone plume is transported across the Atlantic from North-western United States and reaches the eastern part of the British Islands on 17 July (according to both IASI+GOME2 and TCR-2 data, which are not shown). This is supported by 7-day back-trajectories from HYSPLIT (Fig. 9g). This ozone plume shows rather moderate concentrations, and we expect limited impact on the surface ozone concentrations over Europe. We describe this ozone plume here as part of the major ozone outbreak, combining transatlantic and local contributions.

445 The ozone plume coming from the Atlantic is observed on 18 July over Northern Germany by IASI+GOME2 (blue rectangle in Fig. 9a). This is a known hotspot of anthropogenic emissions (Fig. 8a–b). At this stage, these air masses exhibit low CO concentrations but are relatively rich in NO_2. During transport over Northern Europe from 17 to 20 July, the concentrations of ozone, CO, NO_2 and HCHO within this plume gradually increase (blue lines in Fig. 4). Production of ozone during transport is likely enhanced by mixing with local anthropogenic emissions of its precursors.

450 Meanwhile, a large and dense CO plume (but poor in ozone) is depicted by the IASI satellite (Fig. 8d) over the North Sea, which is located north of the ozone plume shown by IASI+GOME2 over Northern Germany (Fig. 9a). This CO plume originates from Central Canada, according to 7-day back-trajectories (Fig. 9h). In this location, TCR-2 reanalyses depict rather weak increases in background concentrations of CO at 850 hPa between the east coast of England and Netherland (Fig. 9c). The simulated plume extends vertically from the lower troposphere (~930 hPa) to the upper troposphere (~240 hPa) with

455 relatively uniform concentration (~110 ppb), thus the total column of CO is larger than the surroundings (as seen by IASI) but not so clearly at a given atmospheric level. Meteorological analyses from ERA5 suggest that the long-range transatlantic transport of these ozone and CO plumes over Northern Europe (~55°N) is likely linked the circulation patterns associated with the Azores anticyclone during the event (see Fig. S2). Similarly, Guerova et al. (2006) found that the frequency of these events depends on the position and strength of the Azores anticyclone.

3.3 Wildfire and biogenic emissions in the Balkan Peninsula

460

The southern branch of ozone plume formed over the Iberian Peninsula at the beginning of the event is transported eastwards over the Western Mediterranean (on 18 July, Fig. 3e and red rectangle in Fig. 9a), exhibiting low CO, NO_2 and HCHO concentrations (red lines in Fig. 4). During the following days, the abundances of these pollutants enhance (Fig. 4) while being transported over Italy and arriving to the Balkan Peninsula on 21 July (Fig. 3f and 10a). Meteorological conditions over Eastern

465 Europe, Italy, and Northern Africa are characterized by extended high pressure, which is accompanied by air subsidence, clear skies, and intense solar heating (Fig. 10f). Heatwave conditions are found over Southern Italy and the Western Balkan Peninsula. This is favourable for ignition and spread of wildfires as well as enhancement of biogenic emissions, as typically occurs over the Mediterranean basin during summer (e.g., Turco et al., 2017). According to MODIS Fire Radiative Power data, wildfires are clearly visible over Central and Southern Italy, and the coast of the Adriatic Sea in the Balkan Peninsula

470 (Fig. 10g). Significant enhancements of CO are seen at this last location (Fig. 10c), probably originating from local wildfires of savannas (the dominant land cover there, Fig. 8e). Moreover, dense plumes of NO_2 and HCHO are simulated over the Balkan Peninsula, from the Adriatic coast and inlands further east (Fig. 10d–e). These regions are characterized by large biogenic emissions (Fig. 8c–d). Meanwhile, low dispersion conditions under the stagnating anticyclonic conditions allow the accumulation of NO_2. Therefore, two sources of ozone precursors are found in this region: wildfires along the Adriatic coast

475 and inland biogenic emissions further east.

Three-days forward-trajectories suggest that a part of the air masses over Eastern Italy move southwards following northerly winds (Fig. 3f–g). Air pollutants likely formed over the Balkan Peninsula are then transported to the Eastern Mediterranean and Northern Africa (Fig. 10a–e). These results suggests that air quality over the Mediterranean may be influenced by eastward transport of ozone pollution from Western Europe and subsequent photochemical production. It is worth noting that previous

480 modelling studies highlighted that regional sources of NO_X and BVOCs are the most important factors controlling summertime ozone in the lower troposphere over the Mediterranean (Richards et al. 2013). The role of transport of air pollutants over the Mediterranean has also been previously remarked. Indeed, the summer circulation over the Eastern Mediterranean is dominated by persistent northerlies known as the Etesians (e.g., Tyrlis et al., 2013). The Etesians are known to have a significant impact on air quality over the Eastern Mediterranean as they transport anthropogenic emissions from European industrial areas

485 (Kalabokas et al., 2008; Lelieveld et al., 2002) and the biomass burning emissions from countries bordering the Black Sea and Southern Europe (de Meji and Lelieveld, 2011; Hodnebrog et al., 2012; Sciare et al., 2008).

3.4 Agricultural burning emission in the north coast of the Black Sea

The three ozone plumes previously monitored while travelling eastwards across Europe (Figs. 3, 10–11) mix into a single large ozone plume that reaches the northern coast of the Black Sea (Romania, Moldavia, Ukraine, and Russia) on 23 July (Fig. 11a–

490 b). Over this region, we can see strong enhancements of CO and relatively weak concentrations of NO_2 and HCHO (Fig. 11c–f). Active biomass burning spots are clearly visible over this region (Fig. 11f), which is mainly covered by croplands (as shown

by Figure 8e). These fires probably correspond to agricultural burning, which is a common practice over Eastern Europe and European Russia for removing crop residuals for new planting or clearing weeds and brushes for grazing. This is the single largest cause (an average of 86%) of the fires detected in Ukraine in 2001–2003 (Korontzi et al., 2006). These events typically occur in July and August, after the harvest of wheat, rye and barley (planted during the previous winter or spring for the last one).

The presence of significant local sources of CO, much likely linked to agricultural burning, are suggested by an increase of its concentration within the polluted plume from ~118 ppb to ~134 ppb during the day of 23 July (Fig. 4c). These local emissions likely mix with the pollutants transported from Western Europe. On other hand, simulated abundances of HCHO and NO_2 do not exhibit remarkable changes during this day (Fig. 4d–e).
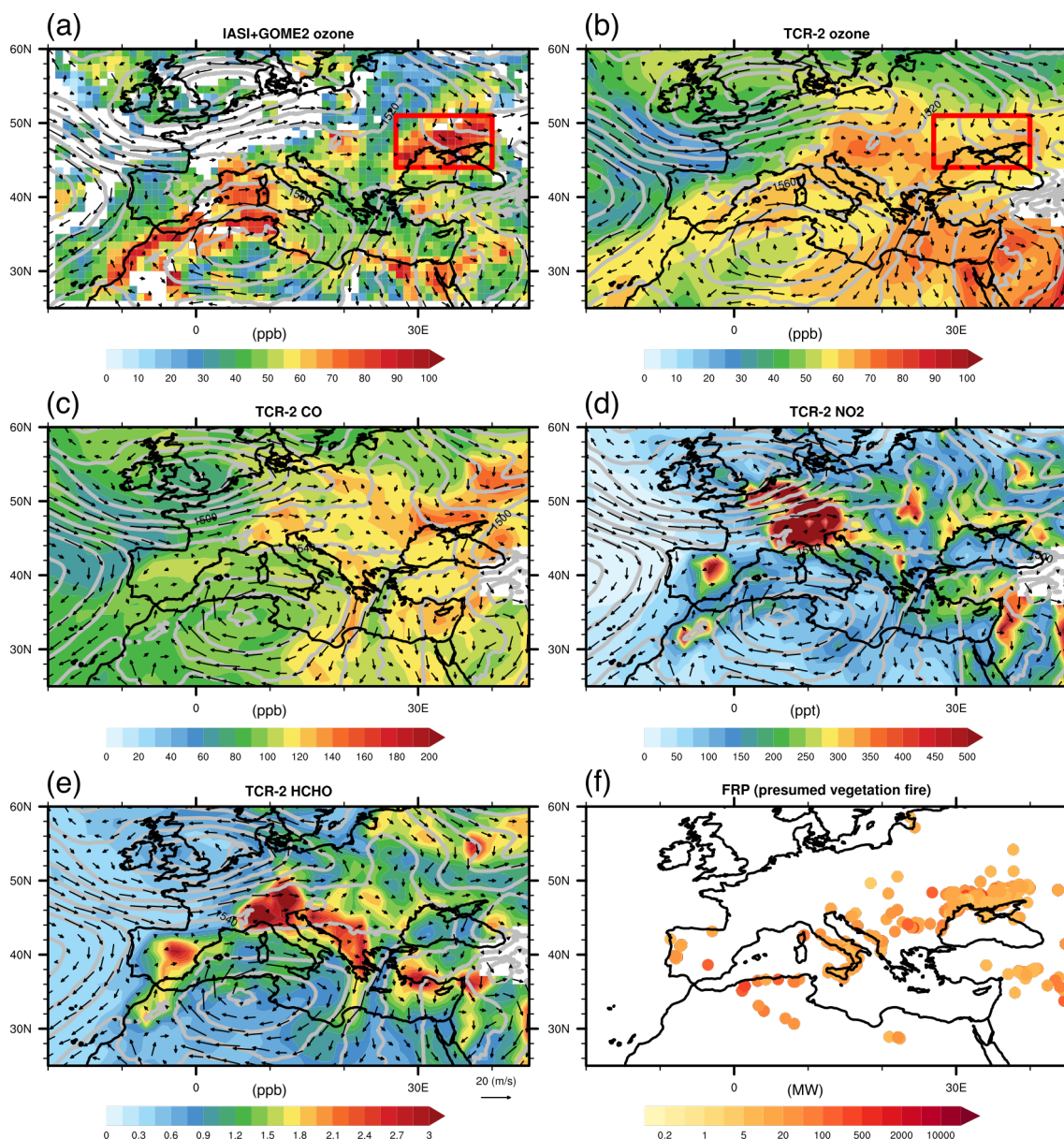
Figure 11: (a–e) Same as Fig. 7a–e and **(f)** Same as Fig. 10f but on 23 July 2017.

505   During the following days, the pollution plume is transported away eastwards from the fire hotspot while the concentrations

of ozone precursors gradually decrease. The temporal variation of ozone observed by IASI+GOME2 within the plume show

different features with respect TCR-2 reanalyses (see Fig. 4a–b). The satellite approach depicts gradual enhancements of ozone

during transport away from the Black Sea coast, suggesting photochemical production of this pollutant, whereas TCR-2

simulates a decrease. These differences are probably associated with the representation of biomass burning emissions and its

510   impact on the simulation of ozone production. Simulations of these processes and their quantification are currently challenging, as shown by the large discrepancies between different state-of-the-art global tropospheric ozone reanalysis products (e.g., Huijnen et al., 2020). Near-surface ozone concentrations are weakly and mainly indirectly constrained by the satellite observations used for assimilation in reanalysis such as TCR-2. In addition, only very few ground-based stations monitor air pollutants over Eastern Europe, as their geographical coverage is far from homogenous across the globe. Particularly in those
515   locations, satellite observations of lowermost tropospheric ozone as those derived by IASI+GOME2 are particularly appreciated for filling the gap of ground-based observations.

4 Conclusions

We have presented a detailed study of the daily evolution and associated sources of precursors of a major ozone outbreak transported across Europe in July 2017, by using IASI+GOME2 multispectral satellite observations and tropospheric chemical
520   reanalysis TCR-2. The multispectral satellite approach offers the currently unique capacity of observing the ozone distribution in the lowermost troposphere (below 3 km a.s.l.), which is in fair consistency with surface observations.

The major European ozone outbreak analysed here is associated with several sources of ozone precursors: biogenic, anthropogenic and biomass burning emissions. We describe the sources of precursors and the transport pathways of these ozone plumes (see scheme in Fig. 12), using IASI+GOME2, TCR-2 and other datasets. At the beginning of the event, warm
525   Saharan air masses are advected northwards over the Iberian Peninsula by the circulation associated with an anticyclone over Morocco, and then heatwave conditions prevailed over the Iberian Peninsula. There, an ozone plume is formed on 16 July 2017, as temperature-induced biogenic emissions increase and collocated high anthropogenic emissions. This ozone plume is co-located with low CO concentrations, but high NO_2 and HCHO abundances. Then, the polluted air plume is transported eastward across the North-western Mediterranean, exhibiting low concentrations of CO, NO_2 and HCHO. These last ones
530   increase as the plume approaches Italy and remain high while reaching the Balkan Peninsula. Over this region, two kinds of sources of ozone precursors are found: wildfire emissions along the coast of the Adriatic Sea and biogenic emissions in the inland region of the Balkan Peninsula.
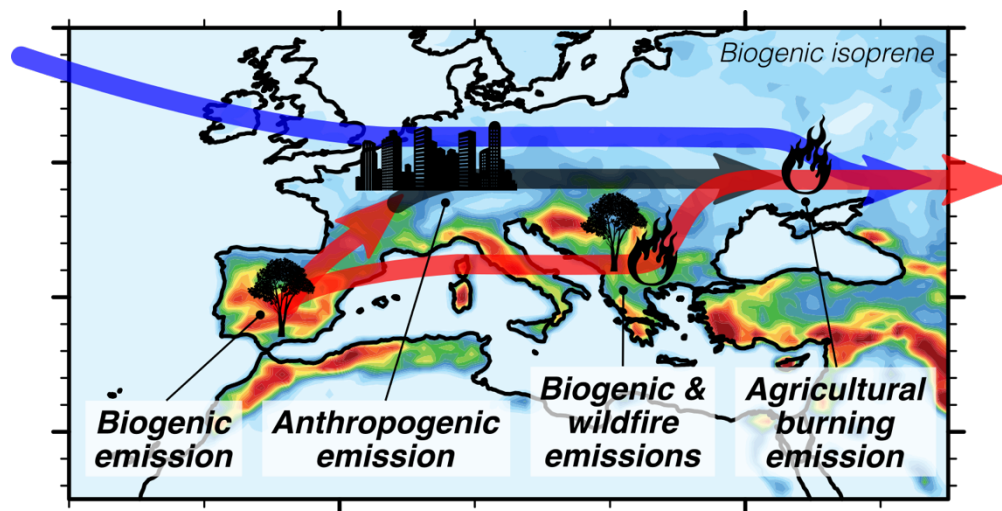
535 **Figure 12:** Schematic of mechanisms that control the major ozone outbreak in July 2017 across Europe.

Meanwhile, two other ozone plumes are also observed over Western and Central Europe. One of them was originally formed over Northern United States and transported across the Northern Atlantic, whereas the other over Eastern France. Both pollution plumes show high concentrations of ozone precursors suggesting a significant impact of anthropogenic emissions
540 from Central Europe. These ozone plumes and the one located over the Balkan Peninsula are transported eastwards and mix gradually into a single large plume which reaches the north coast of the Black Sea. There, active agricultural burning provides with large abundances of precursors, as clearly remarked for CO. The satellite approach highlights significant photochemical production of ozone in the following days, as the polluted air masses are transported further east. Chemical reanalyses did not reproduce this last aspect, which occurred in a remote region and subject to large uncertainties in biomass fire emissions.

545 The multispectral satellite approach IASI+GOME2 has shown original and air-quality-relevant skills to describe the evolution of a major ozone outbreak associated with several sources of ozone precursors across Europe. This capacity is rather unique as explained by a particular enhancement of sensitivity for lowermost tropospheric ozone of this satellite approach. This regional to continental analysis cannot be made with in situ observations only since their spatial coverage is limited. This stresses the contribution of satellite-based approaches for observing ozone pollution provided their highly valuable horizontal
550 coverage.

European anthropogenic emissions of primary air pollutants have been controlled and dropped considerably since the 1990s. Therefore, the contribution of biogenic and biomass burning emissions as precursors of tropospheric ozone is expected to play a significant role locally and on intercontinental transport. Along with global warming, unusually long and intense heatwaves have been become more frequent and severe over Europe (Russo et al., 2015). This is clearly seen in climate model projections
555 at regional and global scales (e.g., Seneviratne et al., 2021). In addition, summer drought conditions and high temperatures are primary drivers of the inter-annual variability of fires (e.g., Turco et al., 2017). It is worth noting that many model

intercomparisons have suggested that anthropogenic emissions are harmonised, but biogenic emissions usually differ from one model to the other (e.g., Im et al., 2015). Generally, state-of-the-art biogenic emissions inventories such as MEGAN tend to overestimate isoprene emissions especially in Scandinavian countries and southwest Europe and underestimate those of

560 monoterpene (e.g., Jiang et al., 2019). It is important for policy and decision making to better observe and understand the response of ozone to change of emissions. Satellite-based approaches can contribute to the quantification of these photochemical processes and highlight remaining gaps in modelling tools, thus their synergism may allow a better understanding air quality degradation and improving the efficiency of pollution mitigation policies.

565 *Acknowledgements*

Authors acknowledge the financial support of Centre National des Etudes Spatiales (CNES, the French Space Agency) via the SURVEYPOLLUTION project from TOSCA (Terre Ocean Surface Continentale Atmosphère), the Université Paris Est Créteil (UPEC), and the Centre National des Recherches Scientifiques–Institut National des Sciences de l'Univers (CNRS-INSU), for helping in achieving this research work and its publication.

570 We thank the French atmospheric data centre AERIS (https://www.aeris-data.fr, last access: 10 June 2022) for supporting the production of IASI+GOME2, data access and computing resources provided by the ESPRI IPSL mesocentre (https://mesocentre.ipsl.fr/, last access: 1 April 2022) and the European Air Quality e-Reporting for in situ surface measurements of ozone, EUMETSAT for GOME-2 level 1 data (provided by the NOAA CLASS data portal). IASI is a joint mission of EUMETSAT and CNES. We thank the Institut für Meteorologie und Klimaforschung (Germany) and RT Solutions

575 (USA) for licenses to use, respectively, the KOPRA and VLIDORT radiative transfer models. We also thank Zhaonan Cai from the Chinese Academy of Sciences (China) and Xiong Liu from the Harvard-Smithsonian Center for Astrophysics (USA) for their help to produce IASI+GOME2 data. The Programme National de Télédétection Spatiale (PNTS) and the Agence Nationale de la Recherche (ANR) also contributed in supporting the development of the IASI+GOME2 satellite product. Part of this work was conducted at the Jet Propulsion Laboratory, California Institute of Technology, under contract with the

580 National Aeronautics and Space Administration (NASA).

We warmly acknowledge all datasets provided for this study: CO satellite retrievals from IASI by ULB/LATMOS (Université Libre de Bruxelles/Laboratoire Atmosphères, Milieux, Observations Spatiales) laboratories (special thanks to C. Clerbaux and J. Hadji-Lazaro), the Terra and Aqua MODIS active fire products by NASA's Fire Information for Resource Management System (FIRMS) (https://earthdata.nasa.gov/firms), part of the NASA Earth Observing System Data and Information System

585 (EOSDIS), MACC-MEGAN, CAMS-GLOB-ANT and CAMS-GLOB-SOIL emission inventories by the Emissions of atmospheric Compounds and Compilation of Ancillary Data (ECCAD) (https://eccad.aeris-data.fr/), the global land cover data by the Land Processes Distributed Active Archive Center (LP DAAC) (https://lpdaac.usgs.gov/), and the aerosol optical depth level 2 data by the Aerosol Robotic Network (AERONET) project (https://aeronet.gsfc.nasa.gov/). We thank Lucas Alados Arboledas, Jose Maria San Atanasio, and Ana Diaz Rodriguez for their effort in establishing and maintaining Granada and

590 Madrid sites of AERONET. We gratefully acknowledge the NOAA Air Resources Laboratory (ARL) for the provision of the
     HYSPLIT transport model used in this publication.

References

Ångström, A.: On the atmospheric transmission of sun radiation and on dust in the air, Geogr. Ann., 11, 156–166,
595   doi:10.1080/20014422.1929.11880498, 1929.

Atkinson, R.: Atmospheric chemistry of VOCs and NO_X, Atmos. Environ., 34, 2063–2101, doi:10.1016/S1352-
       2310(99)00460-4, 2000.

Boersma, K., Eskes, H., Richter, A., De Smedt, I., Lorente, A., Beirle, S., Van Geffen, J., Peters, E., Van Roozen-dael, M.,
       and Wagner, T.: QA4ECV NO_2 tropospheric and stratospheric vertical column data from OMI (Version 1.1) [data set],
600   Royal Netherlands Meteorological Institute (KNMI), https://doi.org/10.21944/qa4ecv-no2-omi-v1.1, 2017a.

Boersma, K., Eskes, H., Richter, A., De Smedt, I., Lorente, A., Beirle, S., Van Geffen, J., Peters, E., Van Roozendael, M., and
       Wagner, T.: QA4ECV NO_2 tropospheric and strato-spheric vertical column data from GOME-2 (Version 1.1) [data set],
       Royal Netherlands Meteorological Institute (KNMI), https://doi.org/10.21944/qa4ecv-no2-gome2a-v1.1, 2017b.

Boersma, K., Eskes, H., Richter, A., De Smedt, I., Lorente, A., Beirle, S., Van Geffen, J., Peters, E., Van Roozendael, M., and
605   Wagner, T.: QA4ECV NO_2 tropospheric and strato-spheric vertical column data from SCIAMACHY (Version 1.1) [data
       set], Royal Netherlands Meteorological Institute (KNMI), https://doi.org/10.21944/qa4ecv-no2-scia-v1.1, 2017c.

Boersma, K. F., Eskes, H. J., Richter, A., De Smedt, I., Lorente, A., Beirle, S., van Geffen, J. H. G. M., Zara, M., Peters, E.,
       Van Roozendael, M., Wagner, T., Maasakkers, J. D., van Der A, R. J., Nightingale, J., De Rudder, A., Irie, H., Pinardi, G.,
       Lambert, J.-C. and Compernolle, S. C.: Improving algorithms and uncertainty estimates for satellite NO_2 retrievals: results
610   from the quality assurance for the essential climate variables (QA4ECV) project, Atmos. Meas. Tech., 11, 6651–6678,
       doi:10.5194/amt-11-6651-2018, 2018.

Bowman, K. W., Rodgers, C. D., Kulawik, S. S., Worden, J., Sarkissian, E., Osterman, G., Steck, T., Lou, M., Eldering, A.,
       Shephard, M., Worden, H., Lampel, M., Clough, S., Brown, P., Rinsland, C., Gunson, M. and Beer, R.: Tropospheric
       Emission Spectrometer: Retrieval method and error analysis, IEEE Trans. Geosci. Remote Sens., 44, 1297–1306,
615   doi:10.1109/TGRS.2006.871234, 2006.

Cai, Z., Liu, Y., Liu, X., Chance, K., Nowlan, C. R., Lang, R., Munro, R. and Suleiman, R.: Characterization and correction
       of global ozone monitoring experiment 2 ultraviolet measurements and application to ozone profile retrievals, J. Geophys.
       Res., 117, D07305, doi:10.1029/2011JD017096, 2012.

Castell, N., Stein, A. F., Salvador, R., Mantilla, E. and Millán, M.: The impact of biogenic VOC emissions on photochemical
620   ozone formation during a high ozone pollution episode in the Iberian Peninsula in the 2003 summer season, Adv. Sci. Res.,
       2, 9–15, doi:10.5194/asr-2-9-2008, 2008.

Chameides, W. and Walker, J. C. G.: A photochemical theory of tropospheric ozone, J. Geophys. Res., 78, 8751–8760, doi:10.1029/JC078i036p08751, 1973.

Colombi, N., Miyazaki, K., Bowman, K. W., Neu, J. L. and Jacob, D. J.: A new methodology for inferring surface ozone from multispectral satellite measurements, Environ. Res. Lett., 16, doi:10.1088/1748-9326/ac243d, 2021.

Crippa, M., Guizzardi, D., Muntean, M., Schaaf, E., Dentener, F., van Aardenne, J. A., Monni, S., Doering, U., Olivier, J. G. J., Pagliari, V. and Janssens-Maenhout, G.: Gridded emissions of air pollutants for the period 1970-2012 within EDGAR v4.3.2, Earth Syst. Sci. Data, 10, 1987–2013, 2018.

Cuesta, J., Eremenko, M., Liu, X., Dufour, G., Cai, Z., Höpfner, M., von Clarmann, T., Sellitto, P., Foret, G., Gaubert, B., Beekmann, M., Orphal, J., Chance, K., Spurr, R. and Flaud, J.-M.: Satellite observation of lowermost tropospheric ozone by multispectral synergism of IASI thermal infrared and GOME-2 ultraviolet measurements over Europe, Atmos. Chem. Phys., 13, 9675–9693, doi:10.5194/acp-13-9675-2013, 2013.

Cuesta, J., Kanaya, Y., Takigawa, M., Dufour, G., Eremenko, M., Foret, G., Miyazaki, K. and Beekmann, M.: Transboundary ozone pollution across East Asia: Daily evolution and photochemical production analysed by IASI + GOME2 multispectral satellite observations and models, Atmos. Chem. Phys., 18, 9499–9525, doi:10.5194/acp-18-9499-2018, 2018.

Cuesta, J., Costantino, L., Beekmann, M., Siour, G., Menut, L., Bessagnet, B., Landi, T. C., Dufour, G. and Eremenko, M.: Ozone pollution during the COVID-19 lockdown in the spring of 2020 over Europe, analysed from satellite observations, in situ measurements, and models, Atmos. Chem. Phys., 22(7), 4471–4489, doi:10.5194/acp-22-4471-2022, 2022.

Cuevas, C. A., Notario, A., Adame, J. A., Hilboll, A., Richter, A., Burrows, J. P. and Saiz-Lopez, A.: Evolution of NO_2 levels in Spain from 1996 to 2012, Sci. Rep., 4, 5887, doi:10.1038/srep05887, 2014.

Curci, G., Beekmann, M., Vautard, R., Smiatek, G., Steinbrecher, R., Theloke, J. and Friedrich, R.: Modelling study of the impact of isoprene and terpene biogenic emissions on European ozone levels, Atmos. Environ., 43, 1444–1455, doi:10.1016/j.atmosenv.2008.02.070, 2009.

de Meij, A. and Lelieveld, J.: Evaluating aerosol optical properties observed by ground-based and satellite remote sensing over the Mediterranean and the Middle East in 2006, Atmos. Res., 99, 415–433, doi:10.1016/j.atmosres.2010.11.005, 2011.

Dee, D. P., Uppala, S. M., Simmons, A. J., Berrisford, P., Poli, P., Kobayashi, S., Andrae, U., Balmaseda, M. A., Balsamo, G., Bauer, P., Bechtold, P., Beljaars, A. C. M., van de Berg, L., Bidlot, J., Bormann, N., Delsol, C., Dragani, R., Fuentes, M., Geer, A. J., Haimberger, L., Healy, S. B., Hersbach, H., Hólm, E. V., Isaksen, L., Kållberg, P., Köhler, M., Matricardi, M., Mcnally, A. P., Monge-Sanz, B. M., Morcrette, J.-J., Park, B.-K., Peubey, C., de Rosnay, P., Tavolato, C., Thépaut, J.-N. and Vitart, F.: The ERA-Interim reanalysis: configuration and performance of the data assimilation system, Q. J. R. Meteorol. Soc., 137, 553–597, doi:10.1002/qj.828, 2011.

Deeter, M. N., Edwards, D. P., Francis, G. L., Gille, J. C., Martínez-Alonso, S., Worden, H. M. and Sweeney, C.: A climate-scale satellite record for carbon monoxide: the MOPITT Version 7 product, Atmos. Meas. Tech., 10, 2533–2555, doi:10.5194/amt-10-2533-2017, 2017.

655   Draxler, R. R. and Hess, G. D.: Description of the HYSPLIT_4 modeling system, NOAA Tech. Memo. ERL ARL-224, NOAA
        Air Resources Laboratory, Silver Spring, MD, 1997.

       Draxler, R. R. and Hess, G. D.: An overview of the HYSPLIT_4 modelling system for trajectories, dispersion and deposition,
        Aust. Meteorol. Mag., 47, 295–308, 1998.

       Draxler, R. R.: HYSPLIT_4 User's Guide, NOAA Tech. Memo. ERL ARL-230, NOAA Air Resources Laboratory, Silver
660   Spring, MD, 1999.

       Dufour, G., Eremenko, M., Griesfeller, A., Barret, B., Leflochmoën, E., Clerbaux, C., Hadji-Lazaro, J., Coheur, P. F. and
        Hurtmans, D.: Validation of three different scientific ozone products retrieved from IASI spectra using ozonesondes,
        Atmos. Meas. Tech., 5, 611–630, doi:10.5194/amt-5-611-2012, 2012.

       EC, Directive 2008/50/EC of the European Parliament and of the Council of 21 May 2008 on ambient air quality and cleaner
665   air   for   Europe   (OJ   L152,   11.6.2008,   p.   1):   https://eur-lex.europa.eu/legal-
        content/EN/TXT/PDF/?uri=OJ:L:2008:152:FULL&from=EN, last access: 14 September 2022, 2008.

       Eck, T. F., Holben, B. N., Reid, J. S., Dubovik, O., Smirnov, A., O'Neill, N. T., Slutsker, I. and Kinne, S.: Wavelength
        dependence of the optical depth of biomass burning, urban, and desert dust aerosols, J. Geophys. Res., 104, 31333–31349,
        doi:10.1029/1999JD900923, 1999.

670   EEA: European Union emission inventory report 1990-2018 under the UNECE Convention on Long-range Transboundary Air
        Pollution (LRTAP), EEA Report No 05/2020, Luxembourg, 2020.

       Eremenko, M., Dufour, G., Foret, G., Keim, C., Orphal, J., Beekmann, M., Bergametti, G. and Flaud, J.-M.: Tropospheric
        ozone distributions over Europe during the heat wave in July 2007 observed from infrared nadir spectra recorded by IASI,
        Geophys. Res. Lett., 35, L18805, doi:10.1029/2008GL034803, 2008.

675   Fehsenfeld, F., Calvert, J., Fall, R., Goldan, P., Guenther, A. B., Hewitt, C. N., Lamb, B., Liu, S., Trainer, M., Westberg, H.
        and Zimmerman, P.: Emissions of volatile organic compounds from vegetation and the implications for atmospheric
        chemistry, Global Biogeochem. Cycles, 6, 389–430, doi:10.1029/92GB02125, 1992.

       Friedl, M., D. Sulla-Menashe.: MCD12C1 MODIS/Terra+Aqua Land Cover Type Yearly L3 Global 0.05Deg CMG V006,
        NASA EOSDIS Land Processes DAAC [Data set], https://doi.org/10.5067/MODIS/MCD12C1.006, 2015.

680   Fu, D., Kulawik, S. S., Miyazaki, K., Bowman, K. W., Worden, J. R., Eldering, A., Livesey, N. J., Teixeira, J., Irion, F. W.,
        Herman, R. L., Osterman, G. B., Liu, X., Levelt, P. F., Thompson, A. M. and Luo, M.: Retrievals of tropospheric ozone
        profiles from the synergism of AIRS and OMI: Methodology and validation, Atmos. Meas. Tech., 11, doi:10.5194/amt-
        11-5587-2018, 2018.

       Garrido-Perez, J. M., Ordóñez, C., García-Herrera, R. and Barriopedro, D.: Air stagnation in Europe: Spatiotemporal
685   variability and impact on air quality, Sci. Total Environ., 645, 1238–1252, doi:10.1016/j.scitotenv.2018.07.238, 2018.

       Garrido-Perez, J. M., Ordóñez, C., García-Herrera, R. and Schnell, J. L.: The differing impact of air stagnation on summer
        ozone across Europe, Atmos. Environ., 219, 117062, doi:10.1016/j.atmosenv.2019.117062, 2019.

Giglio, L., Schroeder, W. and Justice, C. O.: The collection 6 MODIS active fire detection algorithm and fire products, Remote Sens. Environ., 178, 31–41, doi:10.1016/j.rse.2016.02.054, 2016.

690   Graedel, T. E., Bates, T. S., Bouwman, A. F., Cunnold, D., Dignon, J., Fung, I., Jacob, D. J., Lamb, B. K., Logan, J. A., Marland, G., Middleton, P., Pacyna, J. M., Placet, M. and Veldt, C.: A compilation of inventories of emissions to the atmosphere, Global Biogeochem. Cycles, 7, 1–26, doi:10.1029/92GB02793, 1993.

Granier, C., Darras, S., Denier van der Gon, H., Doubalova, J., Elguindi, N., Galle, B., Gauss, M., Guevara, M., Jalkanen, J.-P., Kuenen, J., Liousse, C., Quack, B., Simpson, D. and Sindelarova, K.: The Copernicus Atmosphere Monitoring Service

695   global and regional emissions (April 2019 version), Copernicus Atmosphere Monitoring Service (CAMS) report, Shinfield Park, UK, doi:10.24380/d0bn-kx16, 2019.

Guenther, A. B., Jiang, X., Heald, C. L., Sakulyanontvittaya, T., Duhl, T., Emmons, L. K. and Wang, X.: The model of emissions of gases and aerosols from nature version 2.1 (MEGAN2.1): An extended and updated framework for modeling biogenic emissions, Geosci. Model Dev., 5, 1471–1492, doi:10.5194/gmd-5-1471-2012, 2012.

700   Guerova, G., Bey, I., Attié, J. L., Martin, R. V., Cui, J. and Sprenger, M.: Impact of transatlantic transport episodes on summertime ozone in Europe, Atmos. Chem. Phys., 6, 2057–2072, doi:10.5194/acp-6-2057-2006, 2006.

Guerreiro, C. B. B., Foltescu, V. and de Leeuw, F.: Air quality status and trends in Europe, Atmos. Environ., 98, 376–384, doi:10.1016/j.atmosenv.2014.09.017, 2014.

Herman, R. and Kulawik, S.: Earth Observing System (EOS) Tropospheric Emission Spectrometer TES Level2 (L2) data

705   user's guide (up to & including Version 8 data), JPL D-38042, Pasadena, CA, 2020.

Hersbach, H., Bell, B., Berrisford, P., Hirahara, S., Horányi, A., Muñoz-Sabater, J., Nicolas, J., Peubey, C., Radu, R., Schepers, D., Simmons, A., Soci, C., Abdalla, S., Abellan, X., Balsamo, G., Bechtold, P., Biavati, G., Bidlot, J., Bonavita, M., De Chiara, G., Dahlgren, P., Dee, D., Diamantakis, M., Dragani, R., Flemming, J., Forbes, R., Fuentes, M., Geer, A., Haimberger, L., Healy, S., Hogan, R. J., Hólm, E., Janisková, M., Keeley, S., Laloyaux, P., Lopez, P., Lupu, C., Radnoti,

710   G., de Rosnay, P., Rozum, I., Vamborg, F., Villaume, S. and Thépaut, J. N.: The ERA5 global reanalysis, Q. J. R. Meteorol. Soc., 146, 1999–2049, doi:10.1002/qj.3803, 2020.

Hodnebrog, Solberg, S., Stordal, F., Svendby, T. M., Simpson, D., Gauss, M., Hilboll, A., Pfister, G. G., Turquety, S., Richter, A., Burrows, J. P. and Denier Van Der Gon, H. A. C.: Impact of forest fires, biogenic emissions and high temperatures on the elevated Eastern Mediterranean ozone levels during the hot summer of 2007, Atmos. Chem. Phys., 12, 8727–8750,

715   doi:10.5194/acp-12-8727-2012, 2012.

Hoesly, R. M., Smith, S. J., Feng, L., Klimont, Z., Janssens-Maenhout, G., Pitkanen, T., Seibert, J. J., Vu, L., Andres, R. J., Bolt, R. M., Bond, T. C., Dawidowski, L., Kholod, N., Kurokawa, J., Li, M., Liu, L., Lu, Z., Moura, M. ecilia P., O'Rourke, P. R. and Zhang, Q.: Historical (1750-2014) anthropogenic emissions of reactive gases and aerosols from the Community Emissions Data System (CEDS), Geosci. Model Dev., 11, 369–408, doi:10.5194/gmd-11-369-2018, 2018.

720 Holben, B. N., Eck, T. F., Slutsker, I., Tanré, D., Buis, J. P., Setzer, A., Vermote, E., Reagan, J. A., Kaufman, Y. J., Nakajima, T., Lavenu, F., Jankowiak, I. and Smirnov, A.: AERONET - A federated instrument network and data archive for aerosol characterization, Remote Sens. Environ., 66, 1–16, doi:10.1016/S0034-4257(98)00031-5, 1998.

Horton, D. E., Harshvardhan and Diffenbaugh, N. S.: Response of air stagnation frequency to anthropogenically enhanced radiative forcing, Environ. Res. Lett., 7, 044034, doi:10.1088/1748-9326/7/4/044034, 2012.

725 Hudman, R. C., Moore, N. E., Mebust, A. K., Martin, R. V., Russell, A. R., Valin, L. C. and Cohen, R. C.: Steps towards a mechanistic model of global soil nitric oxide emissions: implementation and space based-constraints, Atmos. Chem. Phys., 12, 7779–7795, doi:10.5194/acp-12-7779-2012, 2012.

Huijnen, V., Miyazaki, K., Flemming, J., Inness, A., Sekiya, T. and G. Schultz, M.: An intercomparison of tropospheric ozone reanalysis products from CAMS, CAMS interim, TCR-1, and TCR-2, Geosci. Model Dev., 13, 1513–1544, 730 doi:10.5194/gmd-13-1513-2020, 2020.

Hunt, B. R., Kostelich, E. J. and Szunyogh, I.: Efficient data assimilation for spatiotemporal chaos: A local ensemble transform Kalman filter, Phys. D Nonlinear Phenom., 230, 112–126, doi:10.1016/j.physd.2006.11.008, 2007.

Hurtmans, D., Coheur, P.-F., Wespes, C., Clarisse, L., Scharf, O., Clerbaux, C., Hadji-Lazaro, J., George, M. and Turquety, S.: FORLI radiative transfer and retrieval code for IASI, J. Quant. Spectrosc. Radiat. Transf., 113, 1391–1408, 735 doi:10.1016/j.jqsrt.2012.02.036, 2012.

Im, U., Bianconi, R., Solazzo, E., Kioutsioukis, I., Badia, A., Balzarini, A., Baró, R., Bellasio, R., Brunner, D., Chemel, C., Curci, G., Flemming, J., Forkel, R., Giordano, L., Jiménez-Guerrero, P., Hirtl, M., Hodzic, A., Honzak, L., Jorba, O., Knote, C., Kuenen, J. J. P., Makar, P. A., Manders-Groot, A., Neal, L., Pérez, J. L., Pirovano, G., Pouliot, G., San Jose, R., Savage, N., Schroder, W., Sokhi, R. S., Syrakov, D., Torian, A., Tuccella, P., Werhahn, J., Wolke, R., Yahya, K., Zabkar, 740 R., Zhang, Y., Zhang, J., Hogrefe, C. and Galmarini, S.: Evaluation of operational on-line-coupled regional air quality models over Europe and North America in the context of AQMEII phase 2. Part I: Ozone, Atmos. Environ., 115, 404–420, doi:10.1016/j.atmosenv.2014.09.042, 2015.

Jacob, D. J. and Winner, D. A.: Effect of climate change on air quality, Atmos. Environ., 43, 51–63, doi:10.1016/j.atmosenv.2008.09.051, 2009.

745 Janssens-Maenhout, G., Crippa, M., Guizzardi, D., Dentener, F., Muntean, M., Pouliot, G., Keating, T., Zhang, Q., Kurokawa, J., Wankmüller, R., Denier van der Gon, H., Kuenen, J. J. P., Klimont, Z., Frost, G., Darras, S., Koffi, B. and Li, M.: HTAP_v2.2: a mosaic of regional and global emission grid maps for 2008 and 2010 to study hemispheric transport of air pollution, Atmos. Chem. Phys., 15, 11411–11432, doi:10.5194/acp-15-11411-2015, 2015.

Jiang, J., Aksoyoglu, S., Ciarelli, G., Oikonomakis, E., El-Haddad, I., Cononaco, F., O'Dowd, C., Ovadnevaite, J., Minguillón, 750 M. C., Baltensperger, U. and Prévôt, A. S. H.: Effects of using two different biogenic emission models on ozone and particles in Europe, Atmos. Chem. Phys., 3747–3768, doi:10.5194/acp-19-3747-2019, 2019.

Kalabokas, P. D., Mihalopoulos, N., Ellul, R., Kleanthous, S. and Repapis, C. C.: An investigation of the meteorological and photochemical factors influencing the background rural and marine surface ozone levels in the Central and Eastern Mediterranean, Atmos. Environ., 42, 7894–7906, doi:10.1016/j.atmosenv.2008.07.009, 2008.

755   Karyampudi, V. M. and Carlson, T. N.: Analysis and numerical simulations of the Saharan Air Layer and its effect on easterly wave disturbances, J. Atmos. Sci., 45, 3102–3136, 1988.

Kew, S. F., Philip, S. Y., van Oldenborgh, G. J., Otto, F. E. L., Vautard, R. and van der Schrier, G.: The exceptional summer heat wave in southern Europe 2017, Bull. Am. Meteorol. Soc., 100(1), 49–53, doi:10.1175/BAMS-D-18-0109.1, 2019.

Kleinman, L. I.: Low and high NO_X tropospheric photochemistry, J. Geophys. Res., 99, 16831–16838,
760   doi:10.1029/94JD01028, 1994.

Korontzi, S., McCarty, J., Loboda, T., Kumar, S. and Justice, C.: Global distribution of agricultural fires in croplands from 3 years of Moderate Resolution Imaging Spectroradiometer (MODIS) data, Global Biogeochem. Cycles, 20, GB2021, doi:10.1029/2005GB002529, 2006.

Lavaysse, C., Cammalleri, C., Dosio, A., van der Schrier, G., Toreti, A. and Vogt, J.: Towards a monitoring system of
765   temperature extremes in Europe, Nat. Hazards Earth Syst. Sci., 18, 91–104, doi:10.5194/nhess-18-91-2018, 2018.

Leibensperger, E. M., Mickley, L. J. and Jacob, D. J.: Sensitivity of US air quality to mid-latitude cyclone frequency and implications of 1980-2006 climate change, Atmos. Chem. Phys., 8, 7075–7086, doi:10.5194/acp-8-7075-2008, 2008.

Lelieveld, J., Berresheim, H., Borrmann, S., Crutzen, P. J., Dentener, F. J., Fischer, H., Feichter, J., Flatau, P. J., Heland, J., Holzinger, R., Korrmann, R., Lawrence, M. G., Levin, Z., Markowicz, K. M., Mihalopoulos, N., Minikin, A., Ramanathan,
770   V., De Reus, M., Roelofs, G. J., Scheeren, H. A., Sciare, J., Schlager, H., Schultz, M., Siegmund, P., Steil, B., Stephanou, E. G., Stier, P., Traub, M., Warneke, C., Williams, J. and Ziereis, H.: Global air pollution crossroads over the Mediterranean, Science, 298, 794–799, doi:10.1126/science.1075457, 2002.

Li, Q., Jacob, D. J., Bey, I., Palmer, P. I., Duncan, B. N., Field, B. D., Martin, R. V., Fiore, A. M., Yantosca, R. M., Parrish, D. D., Simmonds, P. G. and Oltmans, S. J.: Transatlantic transport of pollution and its effects on surface ozone in Europe
775   and North America, J. Geophys. Res., 107, 4166, doi:10.1029/2001JD001422, 2002.

Liu, X., Bhartia, P. K., Chance, K., Spurr, R. J. D. and Kurosu, T. P.: Ozone profile retrievals from the Ozone Monitoring Instrument, Atmos. Chem. Phys., 10, 2521–2537, doi:10.5194/acp-10-2521-2010, 2010.

Livesey, N. J., Read, W. G., Froidevaux, L., Lambert, A., Manney, G. L., Pumphrey, H. C., Santee, M. L., Schwartz, M. J., Wang, S., Cofield, R. E., Cuddy, D. T., Fuller, R. A., Jarnot, R. F., Jiang, J. H., Knosp, B. W., Stek, P. C., Wagner, P. A.
780   and Wu, D. L.: Earth Observing System (EOS) Aura Microwave Limb Sounder (MLS) Version 3.3 Level 2 data quality and description document, JPL D-33509, Pasadena, CA, 2011.

Livesey, N. J., Read, W. G., Froidevaux, L., Lambert, A., Manney, G. L., Pumphrey, H. C., Santee, M. L., Schwartz, M. J., Wang, S., Cofield, R. E., Cuddy, D. T., Fuller, R. A., Jarnot, R. F., Jiang, J. H., Knosp, B. W., Stek, P. C., Wagner, P. A. and Wu, D. L.: Earth Observing System (EOS) Aura Microwave Limb Sounder (MLS) Version 3.3 Level 2 data quality
785   and description document, JPL D-33509 Rev. E, Pasadena, CA, 2020.

Miyazaki, K., Bowman, K., Sekiya, T., Eskes, H., Boersma, F., Worden, H., Livesey, N., Payne, V. H., Sudo, K., Kanaya, Y., Takigawa, M. and Ogochi, K.: Updated tropospheric chemistry reanalysis and emission estimates, TCR-2, for 2005-2018, Earth Syst. Sci. Data, 12(3), 2223–2259, doi:10.5194/essd-12-2223-2020, 2020.

Monks, P. S., Archibald, A. T., Colette, A., Cooper, O., Coyle, M., Derwent, R., Fowler, D., Granier, C., Law, K. S., Mills, G.
790   E., Stevenson, D. S., Tarasova, O., Thouret, V., von Schneidemesser, E., Sommariva, R., Wild, O. and Williams, M. L.: Tropospheric ozone and its precursors from the urban to the global scale from air quality to short-lived climate forcer, Atmos. Chem. Phys., 15, 8889–8973, doi:10.5194/acp-15-8889-2015, 2015.

Orlando, J. J., Tyndall, G. S. and Calvert, J. G.: Thermal decomposition pathways for peroxyacetyl nitrate (PAN): Implications for atmospheric methyl nitrate levels, Atmos. Environ. Part A. Gen. Top., 26, 3111–3118, doi:10.1016/0960-
795   1686(92)90468-Z, 1992.

Pay, M. T., Gangoiti, G., Guevara, M., Napelenok, S., Querol, X., Jorba, O. and García-Pando, C. P.: Ozone source apportionment during peak summer events over southwestern Europe, Atmos. Chem. Phys., 19, 5467–5494, doi:10.5194/acp-19-5467-2019, 2019.

Petetin, H., Thouret, V., Athier, G., Blot, R., Boulanger, D., Cousin, J.-M., Gaudel, A., Nédélec, P., and Cooper, O.: Diurnal
800   cycle of ozone throughout the troposphere over Frankfurt as measured by MOZAIC-IAGOS commercial aircraft, Elem. Sci. Anthr., 4, 000129, https://doi.org/10.12952/journal.elementa.000129, 2016.

Randerson, J. T., van der Werf, G. R., Giglio, L., Collatz, G. J., and Kasibhatla, P. S.: Global Fire Emissions Database, Version 4, (GFEDv4). ORNL DAAC [data set], https://doi.org/10.3334/ORNLDAAC/1293, 2018.

Richards, N. A. D., Arnold, S. R., Chipperfield, M. P., Miles, G., Rap, A., Siddans, R., Monks, S. A. and Hollaway, M. J.: The
805   Mediterranean summertime ozone maximum: Global emission sensitivities and radiative impacts, Atmos. Chem. Phys., 13, 2331–2345, doi:10.5194/acp-13-2331-2013, 2013.

Russo, A., Sousa, P. M., Durão, R. M., Ramos, A. M., Salvador, P., Linares, C., Díaz, J. and Trigo, R. M.: Saharan dust intrusions in the Iberian Peninsula: Predominant synoptic conditions, Sci. Total Environ., 717, 137041, doi:10.1016/j.scitotenv.2020.137041, 2020.

810   Sartelet, K. N., Couvidat, F., Seigneur, C. and Roustan, Y.: Impact of biogenic emissions on air quality over Europe and North America, Atmos. Environ., 53, 131–141, doi:10.1016/j.atmosenv.2011.10.046, 2012.

Schultz, M. G., Schröder, S., Lyapina, O., Cooper, O. R., Galbally, I., Petropavlovskikh, I., von Schneidemesser, E., Tanimoto, H., Elshorbany, Y., Naja, M., Seguel, R. J., Dauert, U., Eckhardt, P., Feigenspan, S., Fiebig, M., Hjellbrekke, A.-G., Hong, Y.-D., Kjeld, P. C., Koide, H., Lear, G., Tarasick, D., Ueno, M., Wallasch, M., Baumgardner, D., Chuang, M.-T., Gillett,
815   R., Lee, M., Molloy, S., Moolla, R., Wang, T., Sharps, K., Adame, J. A., Ancellet, G., Apadula, F., Artaxo, P., Barlasina, M. E., Bogucka, M., Bonasoni, P., Chang, L., Colomb, A., Cuevas-Agulló, E., Cupeiro, M., Degorska, A., Ding, A., Fröhlich, M., Frolova, M., Gadhavi, H., Gheusi, F., Gilge, S., Gonzalez, M. Y., Gros, V., Hamad, S. H., Helmig, D., Henriques, D., Hermansen, O., Holla, R., Hueber, J., Im, U., Jaffe, D. A., Komala, N., Kubistin, D., Lam, K.-S., Laurila, T., Lee, H., Levy, I., Mazzoleni, C., Mazzoleni, L. R., McClure-Begley, A., Mohamad, M., Murovec, M., Navarro-Comas,

820   M., Nicodim, F., Parrish, D., Read, K. A., Reid, N., Ries, L., Saxena, P., Schwab, J. J., Scorgie, Y., Senik, I., Simmonds, P., Sinha, V., Skorokhod, A. I., Spain, G., Spangl, W., Spoor, R., Springston, S. R., Steer, K., Steinbacher, M., Suharguniyawan, E., Torre, P., Trickl, T., Weili, L., Weller, R., Xiaobin, X., Xue, L. and Zhiqiang, M.: Tropospheric Ozone Assessment Report: Database and metrics data of global surface ozone observations, Elem. Sci. Anthr., 5, 58, doi:10.1525/elementa.244, 2017.

825   Sciare, J., Oikonomou, K., Favez, O., Liakakou, E., Markaki, Z., Cachier, H. and Mihalopoulos, N.: Long-term measurements of carbonaceous aerosols in the Eastern Mediterranean: Evidence of long-range transport of biomass burning, Atmos. Chem. Phys., 8, 5551–5563, doi:10.5194/acp-8-5551-2008, 2008.

Seneviratne, S. I., Zhang, X., Adnan, M., Badi, W., Dereczynski, C., Di Luca, A., Ghosh, S., Iskandar, I., Kossin, J., Lewis, S., Otto, F., Pinto, I., Satoh, M., Vicente-Serrano, S. M., Wehner, M. and Zhou, B.: Weather and Climate Extreme Events

830   in a Changing Climate. In Climate Change 2021: The Physical Science Basis. Contribution of Working Group I to the Sixth Assessment Report of the Intergovernmental Panel on Climate Change, edited by Masson-Delmotte, V., Zhai, P., Pirani, A., Connors, S. L., Péan, C., Berger, S., Caud, N., Chen, Y., Goldfarb, L., Gomis, M. I., Huang, M., Leitzell, K., Lonnoy, E., Matthews, J. B. R., Maycock, T. K., Waterfield, T., Yelekçi, O., Yu, R. and Zhou, B., Cambridge University Press, Cambridge, United Kingdom and New York, NY, USA, 1513–1766, doi:10.1017/9781009157896.013, 2021.

835   Sicard, P., De Marco, A., Troussier, F., Renou, C., Vas, N. and Paoletti, E.: Decrease in surface ozone concentrations at Mediterranean remote sites and increase in the cities, Atmos. Environ., 79, 705–715, doi:10.1016/j.atmosenv.2013.07.042, 2013.

Sillman, S., Logan, J. A. and Wofsy, S. C.: The sensitivity of ozone to nitrogen oxides and hydrocarbons in regional ozone episodes, J. Geophys. Res., 95, 1837–1851, doi:10.1029/JD095iD02p01837, 1990.

840   Simpson, D.: Biogenic emissions in Europe: 2. Implications for ozone control strategies, J. Geophys. Res., 100, 22891–22906, doi:10.1029/95JD01878, 1995.

Simpson, D. and Darras, S.: Global soil NO emissions for Atmospheric Chemical Transport Modelling: CAMS-GLOB-SOIL v2.2, Earth Syst. Sci. Data Discuss. [preprint], https://doi.org/10.5194/essd-2021-221, 2021.

Sindelarova, K., Granier, C., Bouarar, I., Guenther, A., Tilmes, S., Stavrakou, T., Müller, J.-F., Kuhn, U., Stefani, P. and Knorr,

845   W.: Global data set of biogenic VOC emissions calculated by the MEGAN model over the last 30 years, Atmos. Chem. Phys., 14, 9317–9341, doi:10.5194/acp-14-9317-2014, 2014.

Solberg, S., Hov, Ø., Søvde, A., Isaksen, I. S. A., Coddeville, P., De Backer, H., Forster, C., Orsolini, Y. and Uhse, K.: European surface ozone in the extreme summer 2003, J. Geophys. Res. Atmos., 113, D07307, doi:10.1029/2007JD009098, 2008.

850   Sousa, P. M., Barriopedro, D., Ramos, A. M., García-Herrera, R., Espírito-Santo, F. and Trigo, R. M.: Saharan air intrusions as a relevant mechanism for Iberian heatwaves: The record breaking events of August 2018 and June 2019, Weather Clim. Extrem., 26, 100224, doi:10.1016/j.wace.2019.100224, 2019.

Stein, A. F., Draxler, R. R., Rolph, G. D., Stunder, B. J. B., Cohen, M. D. and Ngan, F.: NOAA's HYSPLIT atmospheric transport and dispersion modeling system, Bull. Am. Meteorol. Soc., 96, 2059–2077, doi:10.1175/BAMS-D-14-00110.1, 855   2015.

Stohl, A., Bonasoni, P., Cristofanelli, P., Collins, W., Feichter, J., Frank, A., Forster, C., Gerasopoulos, E., Gäggeler, H., James, P., Kentarchos, T., Kromp-Kolb, H., Krüger, B., Land, C., Meloen, J., Papayannis, A., Priller, A., Seibert, P., Sprenger, M., Roelofs, G. J., Scheel, H. E., Schnabel, C., Siegmund, P., Tobler, L., Trickl, T., Wernli, H., Wirth, V., Zanis, P. and Zerefos, C.: Stratosphere-troposphere exchange: A review, and what we have learned from STACCATO, J. 860   Geophys. Res. Atmos., 108, 8516, doi:10.1029/2002jd002490, 2003.

Sun, W., Hess, P. and Liu, C.: The impact of meteorological persistence on the distribution and extremes of ozone, Geophys. Res. Lett., 44, 1545–1553, doi:10.1002/2016GL071731, 2017.

Szopa, S., Naik, V., Adhikary, B., Artaxo, P., Berntsen, T., Collins, W. D., Fuzzi, S., Gallardo, L., Kiendler-Scharr, A., Klimont, Z., Liao, H., Unger, N., and Zanis, P.: Short-Lived Climate Forcers. In Climate Change 2021: The Physical 865   Science Basis. Contribution of Working Group I to the Sixth Assessment Report of the Intergovernmental Panel on Climate Change, edited by: Masson-Delmotte, V., Zhai, P., Pirani, A., Connors, S. L., Péan, C., Berger, S., Caud, N., Chen, Y., Goldfarb, L., Gomis, M. I., Huang, M., Leitzell, K., Lonnoy, E., Matthews, J. B. R., Maycock, T. K., Waterfield, T., Yelekçi, O., Yu, R. and Zhou, B., Cambridge University Press, Cambridge, United Kingdom and New York, NY, USA, 817–922, doi:10.1017/9781009157896.008, 2021.

870   Turco, M., von Hardenberg, J., AghaKouchak, A., Llasat, M. C., Provenzale, A. and Trigo, R. M.: On the key role of droughts in the dynamics of summer fires in Mediterranean Europe, Sci. Rep., 7, 81, doi:10.1038/s41598-017-00116-9, 2017.

Tyrlis, E., Lelieveld, J. and Steil, B.: The summer circulation over the eastern Mediterranean and the Middle East: Influence of the South Asian monsoon, Clim. Dyn., 40, 1103–1123, doi:10.1007/s00382-012-1528-4, 2013.

United States Department of Agriculture/Foreign Agricultural Service/International Production Assessment Division/Country 875   Summary, https://ipad.fas.usda.gov/countrysummary/?id=UP, last access: 05 February 2021, 2020.

Val Martin, M., Honrath, R. E., Owen, R. C. and Lapina, K.: Large-scale impacts of anthropogenic pollution and boreal wildfires on the nitrogen oxides over the central North Atlantic region, J. Geophys. Res., 113, D17308, doi:10.1029/2007JD009689, 2008.

Vautard, R., Honoré, C., Beekmann, M. and Rouil, L.: Simulation of ozone during the August 2003 heat wave and emission 880   control scenarios, Atmos. Environ., 39, 2957–2967, doi:10.1016/j.atmosenv.2005.01.039, 2005.

Vinken, G. C. M., Boersma, K. F., Maasakkers, J. D., Adon, M. and Martin, R. V.: Worldwide biogenic soil NO_X emissions inferred from OMI NO_2 observations, Atmos. Chem. Phys., 14, 10363–10381, doi:10.5194/acp-14-10363-2014, 2014.

Watanabe, S., Hajima, T., Sudo, K., Nagashima, T., Takemura, T., Okajima, H., Nozawa, T., Kawase, H., Abe, M., Yokohata, T., Ise, T., Sato, H., Kato, E., Takata, K., Emori, S. and Kawamiya, M.: MIROC-ESM 2010: model description and basic 885   results of CMIP5-20c3m experiments, Geosci. Model Dev., 4, 845–872, doi:10.5194/gmd-4-845-2011, 2011.

Yan, Y., Pozzer, A., Ojha, N., Lin, J. and Lelieveld, J.: Analysis of European ozone trends in the period 1995-2014, Atmos. Chem. Phys., 18, 5589–5605, doi:10.5194/acp-18-5589-2018, 2018.

Yan, Y., Lin, J., Pozzer, A., Kong, S. and Lelieveld, J.: Trend reversal from high-to-low and from rural-to-urban ozone concentrations over Europe, Atmos. Environ., 213, 25–36, doi:10.1016/j.atmosenv.2019.05.067, 2019.

890 Young, P. J., Archibald, A. T., Bowman, K. W., Lamarque, J.-F., Naik, V., Stevenson, D. S., Tilmes, S., Voulgarakis, A., Wild, O., Bergmann, D., Cameron-Smith, P., Cionni, I., Collins, W. J., Dalsøren, S. B., Doherty, R. M., Eyring, V., Faluvegi, G., Horowitz, L. W., Josse, B., Lee, Y. H., MacKenzie, I. A., Nagashima, T., Plummer, D. A., Righi, M., Rumbold, S. T., Skeie, R. B., Shindell, D. T., Strode, S. A., Sudo, K., Szopa, S. and Zeng, G.: Pre-industrial to end 21st century projections of tropospheric ozone from the Atmospheric Chemistry and Climate Model Intercomparison Project
895 (ACCMIP), Atmos. Chem. Phys., 13, 2063–2090, doi:10.5194/acp-13-2063-2013, 2013.